AGU PUBLICATIONS

JGR

Journal of Geophysical Research: Oceans

RESEARCH ARTICLE

10.1002/2017JC012828

Modeling Arctic sea-ice algae: Physical drivers of spatial distribution and algae phenology

Giulia Castellani[1], Martin Losch[1], Benjamin A. Lange[1,2], and Hauke Flores[1,2]

[1]Alfred Wegener Institute Helmholtz-Zentrum für Polar- und Meeresforschung, Bremerhaven, Germany, [2]Zoological Institute and Zoological Museum, Biocenter Grindel, University of Hamburg, Hamburg, Germany

Key Points:
- Presentation of a new Sea Ice Model for Bottom Algae (SIMBA)
- Study of sea-ice algae phenology as function of physical drivers
- Assessment of the role of ridged ice as a habitat for sea-ice algae

Correspondence to:
G. Castellani,
giulia.castellani@awi.de

Citation:
Castellani, G., M. Losch, B. A. Lange, and H. Flores (2017), Modeling Arctic sea-ice algae: Physical drivers of spatial distribution and algae phenology, *J. Geophys. Res. Oceans*, *122*, doi:10.1002/2017JC012828.

Received 26 FEB 2017
Accepted 23 AUG 2017
Accepted article online 30 AUG 2017

Abstract Algae growing in sea ice represent a source of carbon for sympagic and pelagic ecosystems and contribute to the biological carbon pump. The biophysical habitat of sea ice on large scales and the physical drivers of algae phenology are key to understanding Arctic ecosystem dynamics and for predicting its response to ongoing Arctic climate change. In addition, quantifying potential feedback mechanisms between algae and physical processes is particularly important during a time of great change. These mechanisms include a shading effect due to the presence of algae and increased basal ice melt. The present study shows pan-Arctic results obtained from a new Sea Ice Model for Bottom Algae (SIMBA) coupled with a 3-D sea-ice–ocean model. The model is evaluated with data collected during a ship-based campaign to the Eastern Central Arctic in summer 2012. The algal bloom is triggered by light and shows a latitudinal dependency. Snow and ice also play a key role in ice algal growth. Simulations show that after the spring bloom, algae are nutrient limited before the end of summer and finally they leave the ice habitat during ice melt. The spatial distribution of ice algae at the end of summer agrees with available observations, and it emphasizes the importance of thicker sea-ice regions for hosting biomass. Particular attention is given to the distinction between level ice and ridged ice. Ridge-associated algae are strongly light limited, but they can thrive toward the end of summer, and represent an additional carbon source during the transition into polar night.

1. Introduction

Sea-ice algae are mainly confined to the network of liquid brine inclusions distributed within the ice matrix. This network forms a protected and stable environment. Sea-ice algae are carbon fixers, and constitute an important component of the Arctic marine carbon cycle: almost 60% of primary production in the central Arctic Ocean is attributed to ice algae [*Gosselin et al.*, 1997; *Dupont*, 2012; *Fernández-Méndez et al.*, 2015, 2016]. Moreover, sea-ice algae can represent the majority of the dietary carbon consumption of key Arctic species such as *Calanus glacialis* [*Kohlbach et al.*, 2016]. Through feeding, carbon produced by sea-ice algae is transferred to higher trophic level species such as polar cod *Boreogadus saida*, thus ice algae represent an essential component for the entire Arctic marine food web [*Kohlbach et al.*, 2016, 2017]. As the phytoplankton and ice algal blooms do not coincide in time or space [*Lizotte*, 2001], ice algae may extend the growing and primary production period by 1–3 months [*Jin et al.*, 2012; *Tremblay et al.*, 2008]. Subsequently, the expected changes to timing, magnitude, and spatial distribution of sea-ice algal blooms will likely have a direct impact on higher trophic levels [*Søreide et al.*, 2013; *Wassmann et al.*, 2006]. In an era characterized by a rapidly changing sea ice cover [*Serreze et al.*, 2003, 2007; *Stroeve et al.*, 2007, 2012a, 2012b; *Kwok and Rothrock*, 2009; *Laxon et al.*, 2013; *Haas et al.*, 2008; *Comiso*, 2012; *Nicolaus et al.*, 2012], understanding the temporal and spatial variability of ice-associated biomass and the main physical drivers of algal growth and survival is essential for predicting the fate of sea-ice algae and the consequences on the Arctic marine food web.

Ice algal growth is primarily regulated by light [*Michel et al.*, 1988; *Welch and Bergmann*, 1989] and nutrients [*Cota et al.*, 1987]. Light availability is controlled by incoming shortwave radiation, albedo, sea-ice topography, and snow, whereas nutrients are supplied to the ice algae through brine drainage, in situ regeneration of biogenic material, and exchange with the mixed layer. All these processes are principally regulated by dynamic and thermodynamic processes within sea ice and at the atmosphere-ice and ice-ocean interfaces. Consequently, these processes differ among seasons and regions in the Arctic Ocean. In spring, light transmission is mainly regulated by the snow distribution [*Perovich*, 1996], which in turn is shaped by the surface

undulation as consequence of deformation and differential melt processes [*Iacozza and Barber*, 1999; *Lange et al*., 2017]. In late spring, higher sea-ice temperatures allow brine drainage due to melting. At the same time, the bottom of the ice becomes permeable and this allows exchange of nutrients with the underlying ocean. In summer, after most of the snow has melted, light transmission depends mainly on ice thickness and surface albedo. Still in summer, when the ocean surface is above freezing temperature, basal ice melt represents the largest algal loss [*Grossi et al*., 1987; *Lavoie et al*., 2005]. Ice algae phenology is thus affected by different physical processes depending on season and region, and the spatial distribution of algal biomass at the end of summer is a result of the succession and interplay of different physical processes.

In situ observations in the Arctic, such as sea-ice cores, are difficult to obtain and hence sparse. Moreover, the spatial distribution of algal chl *a* is driven by the succession of physical events preceding the sampling. Additionally, the physical regimes of the sea ice cover are so heterogeneous that it is hard to asses whether the sparse data are representative of the region sampled. In particular, sea-ice environments such as ridged ice and thick old ice are undersampled, thus our understanding of sea-ice algae biogeochemistry is likely biased [*Lange et al*., 2017]. Recent developments in the retrieval of sea-ice algal chl *a* biomass based on under-ice hyperspectral measurements acquired from under-ice profiling platforms, such as Remotely Operated Vehicles (ROV) and the Surface and Under Ice Trawl (SUIT), enabled the retrieval of ice algal chl *a* biomass on scales of meters to kilometers [*Melbourne-Thomas et al*., 2015, 2016; *Lange et al*., 2016; *Meiners et al*., 2017]. Advancements in satellite-based remote sensing during the past decades have vastly improved the monitoring of sea-ice extent [*Stroeve et al*., 2012b; *Ivanova et al*., 2014], thickness [*Kwok et al*., 2009; *Laxon et al*., 2013; *Ricker et al*., 2015; *Tilling et al*., 2015], ocean surface chl *a* concentration, and derived NPP [*Arrigo and van Dijken*, 2011]. Still, ice associated algae and phytoplankton in ice covered regions cannot be observed by satellite, so that a comprehensive picture of their distribution on large scales remains difficult to obtain.

Numerical models can serve as tools to fill the gaps incurred by the methodological difficulties in observing the ice environment. Models can also be used to simulate biogeochemical processes and ice algal dynamics on regional to basin scales, along with their seasonal evolution, and help identify the main physical processes affecting sea-ice algae phenology. Moreover, they are ideal tools for studying possible feedback mechanisms between biological processes and the physical system.

Early sea-ice biogeochemical models were mainly focused on Antarctic sea ice [e.g., *Arrigo et al*., 1993, 1997], and provided the foundation for understanding and modeling mechanisms that drive the seasonality of ecosystems in sea ice [*Arrigo et al*., 1993] and the large-scale algal biomass distribution for the entire sea-ice pack [*Arrigo et al*., 1997]. Modeling efforts since then mainly fall into two categories [*Vancoppenolle and Tedesco*, 2017]: (1) understanding and testing drivers of ecosystems in sea ice [*Arrigo et al*., 1993; *Lavoie et al*., 2005; *Jin et al*., 2006; *Tedesco et al*., 2010; *Saenz and Arrigo*, 2014; *Belém*, 2002; *Mortensen et al*., 2017]; (2) quantifying large-scale quantities, in particular, total biomass and primary production [*Sibert et al*., 2010; *Deal et al*., 2011; *Jin et al*., 2012; *Dupont*, 2012].

In this study, we introduce a simple biogeochemical model for algal growth in a coupled 3-D sea-ice–ocean model of the Arctic Ocean circulation. A model run for 1 year is used to identify the main physical drivers of sea-ice algal growth and decay. The spatial variability of algal chl *a* in late summer is related to the spatial variability of physical sea-ice parameters in the Arctic Ocean. The novelty of this work is the study of sea-ice algae associated to different sea-ice classes. Particular attention is given to ridged and deformed ice, which is difficult to sample and, as a consequence, commonly overlooked as potential algal growth sites [*Kuparinen et al*., 2007; *Meiners et al*., 2012; *Vancoppenolle et al*., 2013; *Lange et al*., 2015]. Finally, possible feedbacks between the ocean–sea-ice system and sea-ice algae are investigated. Our simulations focus on 2012, in order to compare results with observations acquired during late summer of the same year (*Lange* [2016], later referred to as BLROV).

2. Model Description

2.1. Dynamic Sea-Ice–Ocean Model

We use the Massachusetts Institute of Technology general circulation model (MITgcm) in a coupled ocean–sea-ice Arctic Ocean configuration [*Marshall et al*., 1997; *Castro-Morales et al*., 2014]. The domain covers the Arctic Ocean, the Nordic Seas, and the North Atlantic with a southern limit of approximately 50°N. The

horizontal resolution of 1/4° corresponds to a grid spacing of ∼28 km on a rotated spherical grid with the grid equator passing through the geographical North Pole. The ocean is discretized into 33 vertical layers ranging from ∼10 m at the surface to ∼350 m at maximum depth. The ocean model is coupled with a dynamic-thermodynamic sea-ice model [*Losch et al*., 2010]. The sea-ice model uses a viscous-plastic rheology and the so-called zero-layer thermodynamics (i.e., zero heat capacity formulation) [*Semtner*, 1976] with a prescribed ice thickness distribution [*Hibler*, 1979, 1980, 1984; *Castro-Morales et al*., 2014]. The model is forced by atmospheric fields of the NCEP Climate Forecast System Version 2 (CFSv2) for 2012 [*Saha et al*., 2014]. The data set includes fields for 6-hourly wind at 10 m, atmospheric temperature and specific humidity at 2 m, daily downward long and short-radiative fluxes, and a monthly precipitation field. A monthly climatology of river runoff for the main Arctic rivers follows the Arctic Ocean Model Intercomparison Project protocol (AOMIP) [*Proshutinsky et al*., 2001]. The coupled sea-ice–ocean model is spun-up from 1948 to 1978 with the Coordinated Ocean Research Experiment (CORE) Version 2 data and then with the NCEP (CFSv2) from 1979 to the end of 2011.

2.1.1. Ice and Snow Volume Redistribution Due To Ridges

In our configuration, the sea-ice model does not contain a dynamic thickness redistribution function. This means that for each grid cell we know only the mean thickness and there is no explicit information about ridges. In order to differentiate between level ice and ridged ice, we use the energy that accumulates in sea ice due to deformation [*Steiner et al*., 1999; *Castellani*, 2014]. The deformation energy R is the result of internal sea-ice stresses; it is used to estimate the ridge density S_d based on geometrical constraints [*Steiner et al*., 1999] and ice thickness H_i. We use a modified equation from *Steiner et al*. [1999] that avoids unrealistically large numbers of ridges for thickness values lower than 1:

$$S_d = \frac{R}{c_n} \cdot \begin{cases} e^{-\frac{(H_i-1)^2}{0.2}} & \text{for} \quad H_i \leq 1 \\ e^{-\frac{(H_i-1)^2}{3}} & \text{for} \quad H_i > 1 \end{cases} . \tag{1}$$

Table 1 summarizes the parameter values. In order to estimate the ice thickness for level and ridged ice in each grid cell, the following assumptions are made: (1) A ridge is formed by two triangles (sail and keel) sharing the same base. The base is considered to be a rectangle as thick as the parental ice, referred to as grid-averaged sea ice, H_i (Figure 1). (2) The ratio between vertical keel and sail cross-section areas is set to 3.85 [*Timco and Burden*, 1997]. (3) The height of the sail above level ice is estimated to be the same for all ridges with a value of H_{sail}=1.2 m [*Castellani et al*., 2014] and the slope angle of the sides is taken as $\beta = 23°$ [*Steiner et al*., 1999], which gives a ridge base of b_r=5.65 m. The edges of the ridges transmit more light than the central part, where the maximum thickness is found. In order to account for these differences, we redistribute the area of the ridges into a rectangle, and thus we compute an equivalent thickness of H'_r=2.91 m + H_i, where H_i is the thickness of the parental ice (grid-averaged sea ice) and the value 2.91 m is the result of the redistribution of the sail and keel cross section areas into a rectangle. Thus, the thickness of the ridged ice is different for each grid cell due to changes in the grid-averaged sea-ice thickness H_i. The ridges are assumed to be parallel to one of the grid sides, and to extend over the whole length of the grid cell. The ice volume is then redistributed into ridged ice and level ice, giving a thickness of level ice:

$$H_i^l = \frac{H_i - H'_r b_r S_d}{1 - S_d b_r} . \tag{2}$$

All parameters and variables in equations (2) and (3) are listed in Table 1. Ridges are assumed to be practically snow free [*Iacozza and Barber*, 1999; *Sturm et al*., 2002; *Perovich et al*., 2003], so that the snow on level ice has the thickness:

$$H_s^l = \frac{H_s}{1 - S_d b_r} . \tag{3}$$

The distinction between level ice and ridged ice and, as explained in section 2.1.2, their effect on light transmission is used only to drive the algal model (and for diagnostics), but does not affect the thermodynamic and dynamic processes of the model.

2.1.2. Light Attenuation Through Snow and Ice

In the MITgcm, the heat fluxes through ice are computed following *Hibler* [1984]. The mean ice thickness (i.e., the grid-averaged sea-ice thickness) is distributed into seven ice thickness categories between 0 and a

Table 1. List of Variables and Parameters, and Corresponding Description and Units Used in the Model[a]

Variable	Definition	Computed/Read	Unit
B	Ice algal biomass concentration	Computed	mg chl a m^{-3}
D	Detritus concentration	Computed	mg m^{-3}
F_{ia}	Energy released as heat by sea-ice algae	Computed	W m^{-2}
H_i	Ice thickness	Computed	m
H_s	Snow thickness	Computed	m
H_i^l	Thickness of level ice	Computed	m
H_s^l	Thickness of snow on level ice	Computed	m
H_r'	Thickness of ridged ice	Computed	m
I_0	Shortwave incoming radiation	External field	W m^{-2}
k_B	Algae attenuation coefficient	Computed	m^{-1}
$\tilde{M}$	Melt rate at the bottom of sea ice	Computed	m s^{-1}
$\tilde{M}_B$	Bottom melt caused by heat released by algae	Computed	m s^{-1}
μ	Growth rate	Computed	day^{-1}
N	Nitrate concentration	Computed	mg m^{-3}
PAR	Photosynthetic active radiation	Computed	μEinst m^{-2} s^{-1}
R	Deformation energy	Computed	J m^{-2}
S_d	Ridge density	Computed	nr m^{-1}
Parameter	Definition	Value	Unit
α	Albedo	See Table 2	Dimensionless
a^*	Mean chl a specific attenuation coefficient[a)]	0.02	m^2 (mg chl a)$^{-1}$
α_B	Photosynthetic efficiency[a)]	0.07	mg C (mg chl a)$^{-1}$ h^{-1} (μEinst m^{-2} s^{-1})$^{-1}$
b_r	Base length of ridges	5.65	m
C_0	Surface transmission parameter[b)]	0.3	Dimensionless
c_n	Proportionality constant for ridge density calculation[c)]	14×10^3	J$^{1/2}$ m$^{-1/2}$
δz	Bottom layer occupied by sea-ice algae[a)]	0.05	m
F_r	Fraction of absorbed energy released as heat by algae[d)]	0.9	Dimensionless
k_N	Half saturation constant for nitrate uptake[e)]	0.1	mg m^{-3}
k_i	Ice attenuation coefficient[a,f)]	1.5	m^{-1}
k_s	Snow attenuation coefficient[f)]	5	m^{-1}
L_i	Latent heat of fusion of sea ice[d)]	283	KJ kg^{-1}
λ_{mo}	Mortality rate[g)]	0.02	day^{-1}
$\lambda_{up/re}$	Uptake and respiration rate[g)]	0.01	day^{-1}
λ_{rm}	Remineralization rate[g)]	0.01	day^{-1}
μ_M	Maximum ice algal specific growth rate[h)]	0.86	day^{-1}
P_m	Maximum photosynthetic rate[a)]	0.28	mg C (mg chl a)$^{-1}$ h^{-1}
ρ_i	Sea ice density[i)]	910	kg m^{-3}

[a]Variables are marked as computed by the model or read as external field. Parameters superscript refers to the source: a) *Lavoie et al.* [2005], b) *Grenfell and Maykut* [1977], c) *Steiner et al.* [1999], d) *Zeebe et al.* [1996], e) *Sarthou et al.* [2005], f) *Perovich* [1996], g) tuned with 1-D experiments, h) *Vancoppenolle and Tedesco* [2017], and i) as in the MITgcm.

maximum thickness of twice the mean thickness. The distribution of these seven thicknesses is flat, normalized and fixed in time [see *Hibler*, 1984; *Castro-Morales et al.*, 2014, Figure 1]. The snow follows the same thickness distribution so that thin ice is covered by a thin snow layer and thick ice by a thick snow layer [*Castro-Morales et al.*, 2014]. The heat flux is computed for each thickness category. Then all the heat fluxes are averaged to give the net heat flux that is responsible for thermodynamic processes such as basal melting or freezing. Note that in this subgrid parameterization, some part of the grid always contains thin ice of

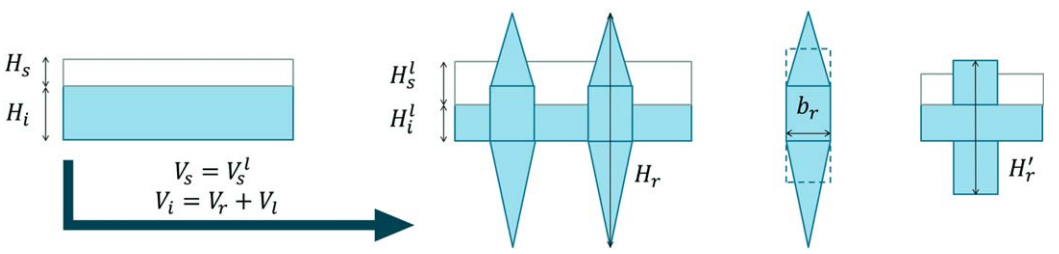

Figure 1. Scheme of grid-averaged sea-ice volume (V_i) and snow volume (V_s) redistribution into level ice volume and level snow volume (V_l and V_s^l) and ridged ice volume (V_r). The notation refers to: grid-averaged sea-ice thickness (also called parental ice) H_i; snow thickness on grid-averaged sea ice H_s; level sea-ice thickness H_i^l and snow thickness on level ice H_s^l; total thickness H_r and base b_r of ridges; final thickness of ridges $H_r' = 2.91\ \text{m} + H_i$ (see also section 2.1.1).

Table 2. Values for Albedo as a Function of Surface (Ice and Snow) Conditions Used in the Sea-Ice Package of the MITgcm

Surface Conditions	Albedo α
Dry ice	0.70
Wet ice	0.68
Dry snow	0.81
Wet snow	0.77

$\frac{1}{7}$ the mean thickness, which allows a finite heat flux even for thick mean ice. The light transmission through each thickness category follows the Beer-Lamber law:

$$I^{(c)}\left(H_i^{(c)}, H_s^{(c)}\right) = I_0(1-\alpha)C_0 e^{-k_i H_i^{(c)} - k_s H_s^{(c)}}, \tag{4}$$

where $H_i^{(c)}$ and $H_s^{(c)}$ are the ice thickness and snow thickness of category c, I_0 the incoming shortwave radiation, and α the albedo. The albedo depends on snow and ice types, as listed in Table 2. The surface transmission parameter $C_0=0.3$ accounts for that part of incoming radiation absorbed in the first few centimeters of the ice [*Grenfell and Maykut*, 1977]. k_i and k_s are constant attenuation coefficients for sea ice and snow [*Lavoie et al.*, 2005]. For a detailed review of ice and snow attenuation coefficients see *Perovich* [1996]. In our study, the algae are assumed to occupy only a bottom layer of 5 cm of the sea ice [*Vancoppenolle and Tedesco*, 2017; *Lavoie et al.*, 2005; *Jin et al.*, 2006; *Dupont*, 2012] (see section 2.2) so that there is no self-shading effect due to ice algae above the bottom layer.

The light transmission through grid-averaged sea ice is computed according to equation (4) with the same values of k_i and k_s (Table 1) for each thickness category. The transmitted shortwave radiation (light) fluxes are summed to give the net shortwave heat flux that penetrates into the ocean. In the case of the redistributed ice into level and ridged ice (section 2.1.1), the light transmission through level ice, excluding the ridges, is computed in accordance to the grid-averaged ice with the same attenuation parameters and using the same thickness distribution. Ridged ice is assumed to occupy only one separate category for which we assume a smaller $k_i=0.8$ m^{-1} due to the higher porosity of ridges. To avoid any confounding effects, the ocean is not affected by the modified light transmission based on the redistribution into level ice and ridged ice.

2.2. SIMBA: Sea Ice Model for Bottom Algae

The new Sea Ice Model for Bottom Algae (SIMBA) has one class of algae, one for nutrients and one for detritus. Nitrate represents the nutrients because it is typically considered the limiting nutrient for ice algal growth in fully marine waters [*Smith et al.*, 1997]. We assume that the ice algae occupy a bottom layer of thickness δz of 5 cm [see also *Lavoie et al.*, 2005; *Jin et al.*, 2006; *Dupont*, 2012; *Lange et al.*, 2015]. We consider four main biological processes responsible for changes in algae, nutrient and detritus concentrations: uptake of nutrients from the algae, respiration transforming algae back into nutrients, mortality of algae that are then transformed into detritus, and remineralization, which describes the decomposition of organic matter, i.e., detritus converted back into nutrients. The physical processes affecting algae, nutrient and detritus are light limitation, sea-ice basal melting (melting of ice results in removal of ice algae), and horizontal transport of ice (algae are advected as tracers in sea ice). A term for the resupply of nutrients from the underlying ocean water is not considered in the present configuration. The equations solved by the model for ice algae biomass B, nutrient N and detritus D are:

$$\frac{dN}{dt} = -(\mu - \lambda_{up/re})B + \lambda_{rm} D, \tag{5}$$

$$\frac{dB}{dt} = (\mu - \lambda_{up/re})B - \lambda_{mo} B + \frac{\tilde{M}}{\delta z} B, \tag{6}$$

$$\frac{dD}{dt} = \lambda_{mo} B - \lambda_{rm} D. \tag{7}$$

A term for algal loss due to melting is considered in equation (6) where $\tilde{M}$ is the basal melt rate (m s^{-1}). Melt loss of algae is the only flux of material to the underlying ocean waters. Parameters describing respiration ($\lambda_{up/re}$), mortality (λ_{mo}) and remineralization (λ_{rm}) are assumed to be constant (see Table 1).

The growth rate μ is a function of nutrient availability $f(N)$ and light availability $f(PAR)$:

$$\mu = \mu_M f(N) f(PAR). \tag{8}$$

The term μ_M is a constant and represents the maximum growth rate (see Table 1). The limitation of photosynthesis by nutrient supply is assumed to follow a Michaelis-Menten form [*Monod*, 1949]:

$$f(N)=\frac{N}{N+k_N}, \tag{9}$$

where $k_N=0.1$ mg m^{-3} is the half saturation constant for nitrate [*Sarthou et al*., 2005]. The response of photosynthesis to light follows *Webb et al*. [1974]:

$$f(PAR)=1-e^{-\frac{\alpha_B PAR}{P_m}}, \tag{10}$$

where PAR (Photosynthetically Active Radiation) is that part of the light spectrum used for photosynthesis, α_B is the photosynthetic efficiency and P_m is the light saturated specific photosynthetic rate (or maximum photosynthetic rate). Values for α_B and P_m (Table 1) are taken as averages of the values suggested in *Lavoie et al*. [2005], their Table 2. To convert light I from W m^{-2} into PAR in μEinst m^{-2} s^{-1}, we follow *Vancoppenolle et al*. [2011] and *Lavoie et al*. [2005]:

$$PAR=0.45\cdot 4.91\cdot I, \tag{11}$$

where 4.91 is the quanta-energetic ratio and 0.45 is the ratio between total number of incoming quanta in the visible region (0.4–0.7 μm) with respect to the number for the entire shortwave (0.3–3 μm) band [*Frouin and Pinker*, 1995].

The response of the algal model to the physical forcings provided by the sea-ice–ocean system for 2012 was tested with 1-D experiments (not shown). SIMBA is then applied to the entire Arctic basin in two different study cases: (1) the case of grid-averaged sea-ice thickness (section 3.1), used also to investigate the effects of algae on the sea-ice–ocean system (section 3.2); and (2) the case of distinction between level ice and ridged ice (section 3.3).

2.3. Effects on Ice and Ocean Systems

Since light is also needed for phytoplankton growth under sea ice, the presence of algae at the bottom might inhibit or delay the under-ice phytoplankton bloom in the surface ocean. In order to test such an effect, we estimate the light that reaches the ocean surface following *Lavoie et al*. [2005] and previously *Kirk* [1983] as a function of sea-ice algae chl *a* concentration. The attenuation coefficient due to algae k_B is

$$k_B=a^*\cdot B, \tag{12}$$

with $a^*=0.02$ m^2 (mg chl a)$^{-1}$. Adding this term into equation (4) we get:

$$I(H_i,H_a,\text{chl } a)=I_0(1-\alpha)C_0e^{-k_iH_i-k_sH_s-k_B\delta z}. \tag{13}$$

Ice algae absorb more PAR than that required for photosynthesis. The extra energy is released as heat, thus contributing to basal ice melt. To quantify such algae-induced melt, we follow *Lavoie et al*. [2005]:

$$\tilde{M}_B=\frac{I(H_i,H_s)\,F_r\,(1-e^{-k_B\delta z})}{\rho_i L_i}, \tag{14}$$

where F_r is the fraction of the energy absorbed by the ice algal layer that is released as heat, L_i is the latent heat for sea ice and ρ_i the density of sea ice. Values for F_r and L_i are taken from *Zeebe et al*. [1996] and listed in Table 1. These effects are diagnosed and discussed in section 3.2, but in our first version of SIMBA they do not feed back into SIMBA nor the ocean and sea-ice physics.

3. Results

3.1. SIMBA Applied to Grid-Averaged Sea Ice

In Figures 2 and 3, we show the simulated sea-ice concentration and the sea-ice thickness for September 2012, respectively. Areas of interest for our study are also highlighted. We run the coupled algae–sea-ice–ocean model in a 3-D configuration accounting for five different scenarios R0, R2, R4, R6, and R8 representing five different initial conditions (see Table 3). This first comparison allows us to identify the run which has the best agreement with observations, but also to test the sensitivity to different initial conditions.

For a quantitative comparison, we use sea-ice algal chl *a* estimates by BLROV (Table 4). We limit our comparison to the median values shown in Table 1 (Chapter 3) of BLROV to have the most representative

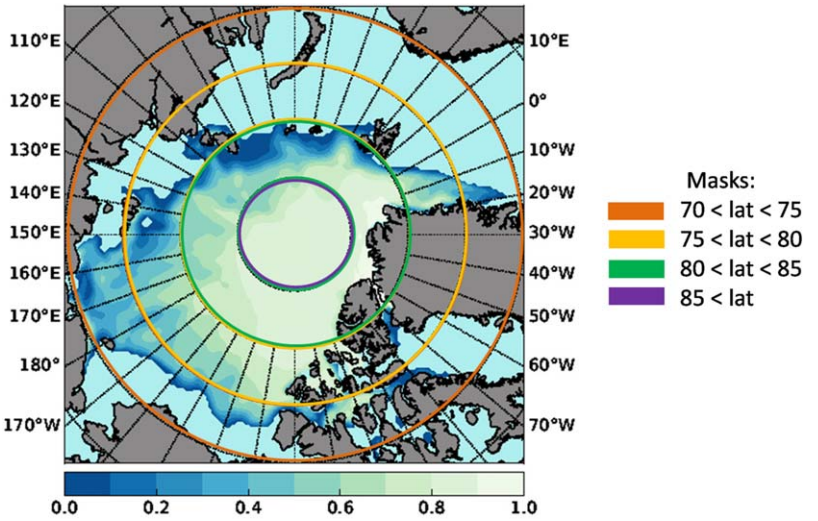

Figure 2. Map of the model domain with white-blue shades corresponding to the simulated sea-ice concentration in September 2012. The colored rings represent the masking applied to the domain according to latitude, as explained in section 3.

measurements for comparison with model output on a grid of 1/4°. There are two reasons why we focus our comparison mainly on BLROV data. First, the data were collected in 2012 and allow a direct comparison in time and space. Second the chl *a* estimates are based on under-ice hyperspectral radiation measurements [*Lange et al.*, 2016] conducted with a ROV over a scale of hundreds of meters, so that they are not point-measurements and relate better to the grid-cell averages (∼25 km) of the model. A qualitative comparison with empirical data is discussed in section 4.

The chl *a* estimates from BLROV are binned in three areas of interest (Figure 3), namely Marginal Ice Zone (MIZ), Transitional Area (TA) and Compact Area (CA). The averaged data and the corresponding model values in the same three regions for the five different initial conditions are listed in Table 3. Amongst the five runs, R4 shows the best agreement to observations, thus hereafter our analysis will be restricted to the R4 run, except when stated otherwise.

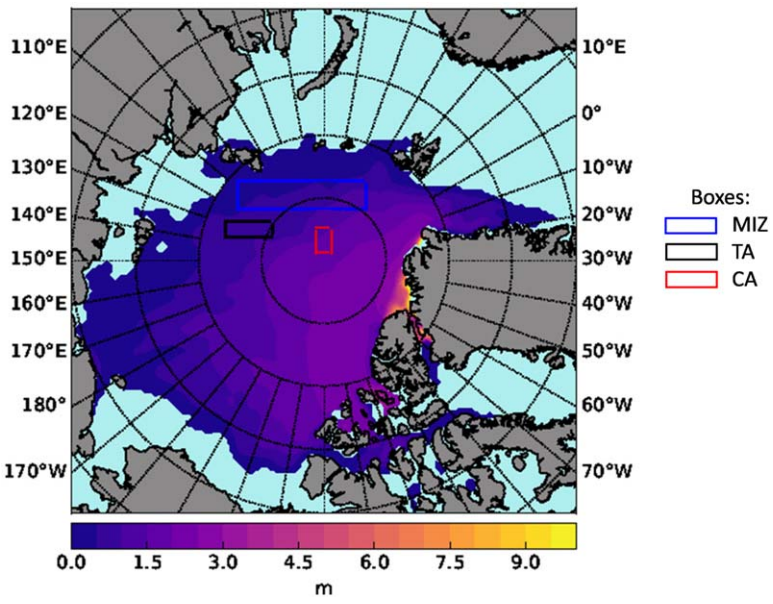

Figure 3. Map of the model domain with grid-averaged sea-ice thickness for September 2012 depicted by colors. The square boxes represent the areas considered for a comparison with observations (section 3): Marginal Ice Zone (MIZ), Transitional Area (TA), and Compact Area (CA).

Table 3. Initial Conditions (mg m^{-2}) for Sea-Ice Algae (B), Nutrient (N), and Detritus (D) in Five Different Scenarios (R0, R2, R4, R6, and R8), and Mean Values of Algal Chl *a* Concentrations (mg m^{-2}) to be Compared With Observations in Three Different Regions (See Also Figure 3): Marginal Ice Zone (MIZ), Transitional Area (TA), and Compact Area (CA)[a]

	Initial Conditions (mg m^{-2})			Model Predicted Mean Chl *a* per Region (mg m^{-2})		
Run	B	N	D	MIZ	TA	CA
R0	50	0.74	0	0.61	0.82	1.32
R2	0.05	50	0	0.76	0.98	1.33
R4	0.05	50	25	1.24	1.57	2.14
R6	0.05	25	25	0.87	1.09	1.51
R8	0.05	0.74	50	0.98	1.21	1.69
Obs				1.23	1.94	4

[a]The chl *a* values are averages for September to be compared with observations. The last row contains the median values from Table 4 to allow an easier comparison with modeled values.

In September, simulated and observed algae concentrations appear to be low in the Marginal Ice Zone (Figure 4). The modeled concentrations increase approximately with latitude and reach a maximum in the Lincoln Sea with values exceeding 10 mg chl *a* m^{-2}. North of 85°N the algae concentration increases from the eastern sector to the western sector from 1.29 to 4.33 mg chl *a* m^{-2}. The observed mean value for that region is higher (Table 3) with 4 mg chl *a* m^{-2} compared to a mean modeled value of 2.81 mg chl *a* m^{-2}, but still in the range of variability.

In summer (between April and September), more than 1 m of ice melts in the MIZ (Figure 5), but melt rates are low in multiyear ice regions along the coast of Greenland and north of the Canadian Arctic Archipelago (CAA). In particular, the total melt in the Lincoln Sea is 1 order of magnitude smaller than in the marginal sea-ice zone.

In Figure 6, we show the spring to autumn evolution of under-ice light, sea-ice algal biomass, nutrients and detritus for four different latitudinal regions between 70°N to 75°N, 75°N to 80°N, 80°N to 85°N, and greater than 85°N (Figure 2). Table 5 lists key numbers that characterize the experiments: (1) bloom onset defined as the day when the algae start to grow exponentially, inferred from the slope of the curves in Figure 6b; this corresponds to (2) a threshold for PAR to trigger the bloom, i.e., above such value an algal bloom develops; (3) the day when the peak of biomass is reached, identified as the maximum of the curve (Figure 6b); (4) the maximum biomass value. We note, that the threshold value for PAR should not be confused with the threshold for algal growth, since the algae start growing already at lower values.

Onset of algal bloom and time of maximum biomass differ from region to region (Figure 6 and Table 5). South of 75°N, the growth becomes exponential already at the end of March (day 87), followed by more northern regions. For the area north of 85°N, bloom onset is 40 days later than in the southernmost region. A similar delay is seen in the timing of maximum biomass with a gap of 30 days between the southernmost sector and the northernmost sector. Note, that the bloom in the region north of 85°N develops faster, reaching its maximum in 21 days compared to ~33 days for the other regions. North of 85°N the maximum algal biomass is also larger, with 50 mg chl *a* m^{-2} compared to the mean of ~36 mg chl *a* m^{-2} in other regions. After the peak, algae start dying and reach a minimum at the end of August. There is also a secondary growth period between September and October, before algal biomass decreases to its minimum (Figure 6b). This feature has also been reported in other models [*Jin et al.*, 2006; *Deal et al.*, 2011; *Jin et al.*, 2012; *Ji et al.*, 2013] and attributed to the detritus compartment. Before the spring bloom, nutrient concentrations increase slightly (Figure 6c) as inorganic matter remineralizes. When the bloom initiates, algae consume nutrients until they become nutrient limited. The detritus increases when algae die.

Table 4. Sea-Ice Algal Chl *a* (mg m^{-2}) From BLROV[a]

Study Area	Median (mg chl *a* m^{-2})	75% Median (mg chl *a* m^{-2})	IQR25 (mg chl *a* m^{-2})	IQR75 (mg chl *a* m^{-2})
MIZ	1.23	0.86	1.15	1.36
TA	1.94	1.46	1.66	2.32
CA	4	3	2.15	6.7

[a]Measurements were undertaken at the end of August and in September 2012, the locations are shown in Figure 4. Values are averaged according to region (see also Figure 3) and refer to median, 75% of median (assuming that 75% of the total biomass lies in the bottom part), 25th percentile (IQR25), and 75th percentile (IQR75).

The day of bloom onset depends on light availability and therefore on latitude (Figure 7a), but light availability is also affected by other factors. The spatial pattern of these factors, i.e., snow thickness, ice thickness and snow melt (Figures 7b–7d), are remarkably similar to the bloom onset pattern. From Figure 7a we see an increasing trend from the Bering Strait to the region north of 85°N, with day of bloom onset going from 90 to 135. The areas that do not follow this latitudinal dependence

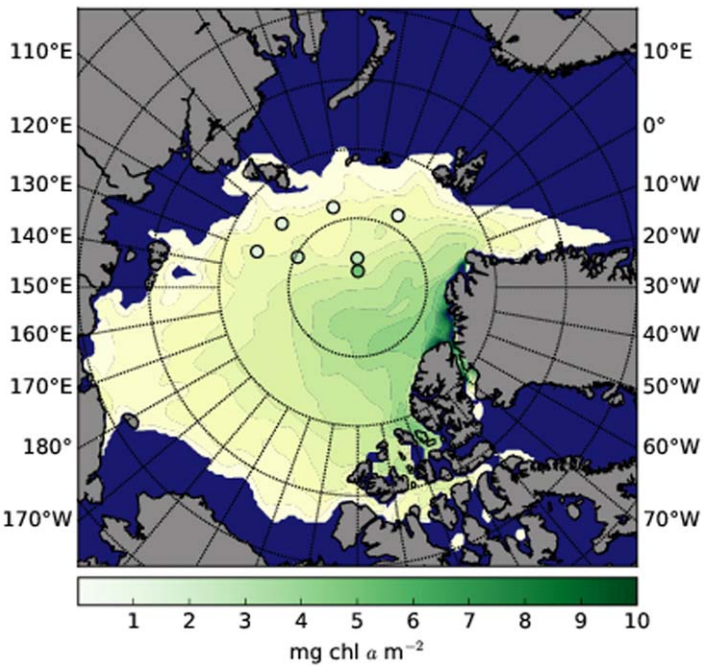

Figure 4. Pan Arctic map of sea-ice algal chl *a* concentration per grid cell simulated for September 2012. The circles represent the ROV-based observations from BLROV (see section 3). Both observed and simulated values use the same color scale.

are the Kara Sea, Fram Strait and Lincoln Sea. The day of complete snow melt (Figure 7b) shows values around 130 in the Beaufort Sea and East Siberian Sea, whereas values are up to 180 for latitudes larger than 85°N and in the Nansen Basin. Ice thickness (Figure 7c) is in the range 0.5–3.5 m in most of the Arctic Ocean, hence in agreement with observations [*Ricker et al.*, 2017], except for the Lincoln Sea, where thicknesses of up to 10 m represent an overestimation compared to recent satellite data [*Ricker et al.*, 2017]. Snow thickness ranges between 10 and 40 cm in the Beaufort Sea, East Siberian Sea, and Laptev Sea, whereas values are up to 1 m in the Nansen Basin and Kara Sea close to Severnaya Zemlya islands.

Monthly values of net primary production NPP are shown in Figure 8. NPP has a maximum value around 15 mg C m^{-2} d^{-1}. The spatial patterns between April and July resemble the latitudinal dependency of the algal bloom. In April and May values are higher at the marginal areas than in the central Arctic, whereas the situation is reversed in June and July. The end of July sees the termination of the major production season in sea ice.

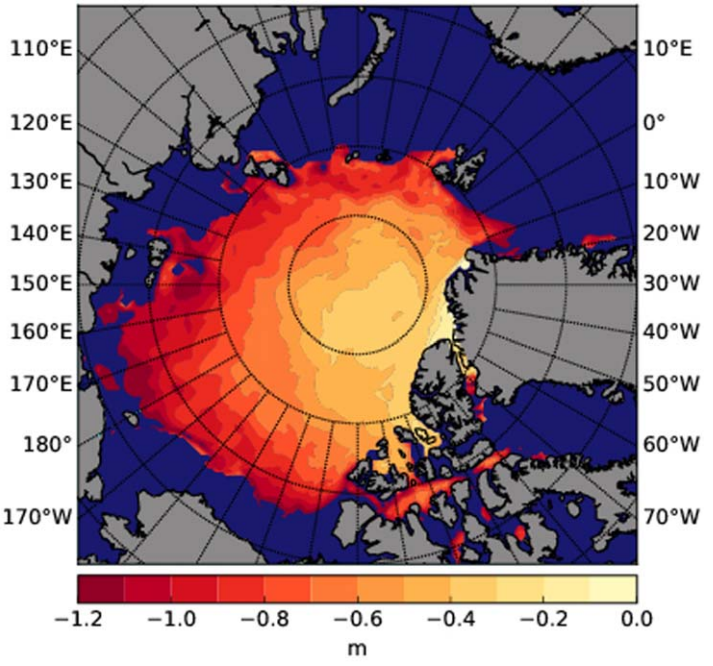

Figure 5. Total summer basal ice melt (m) integrated over the period April to September 2012 obtained from the sea-ice model.

3.2. Estimating Effects on Ice and Ocean Physics

Algae at the bottom of sea ice absorb light and hence reduce light penetration through the ice into the ocean surface. In the two latitudinal bands between 70°N, 75°N, and 80°N the light reaching the surface ocean (Figure 9a) remains very close to the mean threshold value (gray line in Figure 9a) inferred from the light regime without the shading effect (Figure 6a). In the latitudinal bands north of 80°N, the light remains under the threshold value until mid-June. The shading effect is nearly zero before April and then increases to values up to 2 μEinst m^{-2} s^{-1}, or 20–30% of the transmitted radiation, in June and July (Figure 9b).

Integrated summer (April to September) algae-induced melt

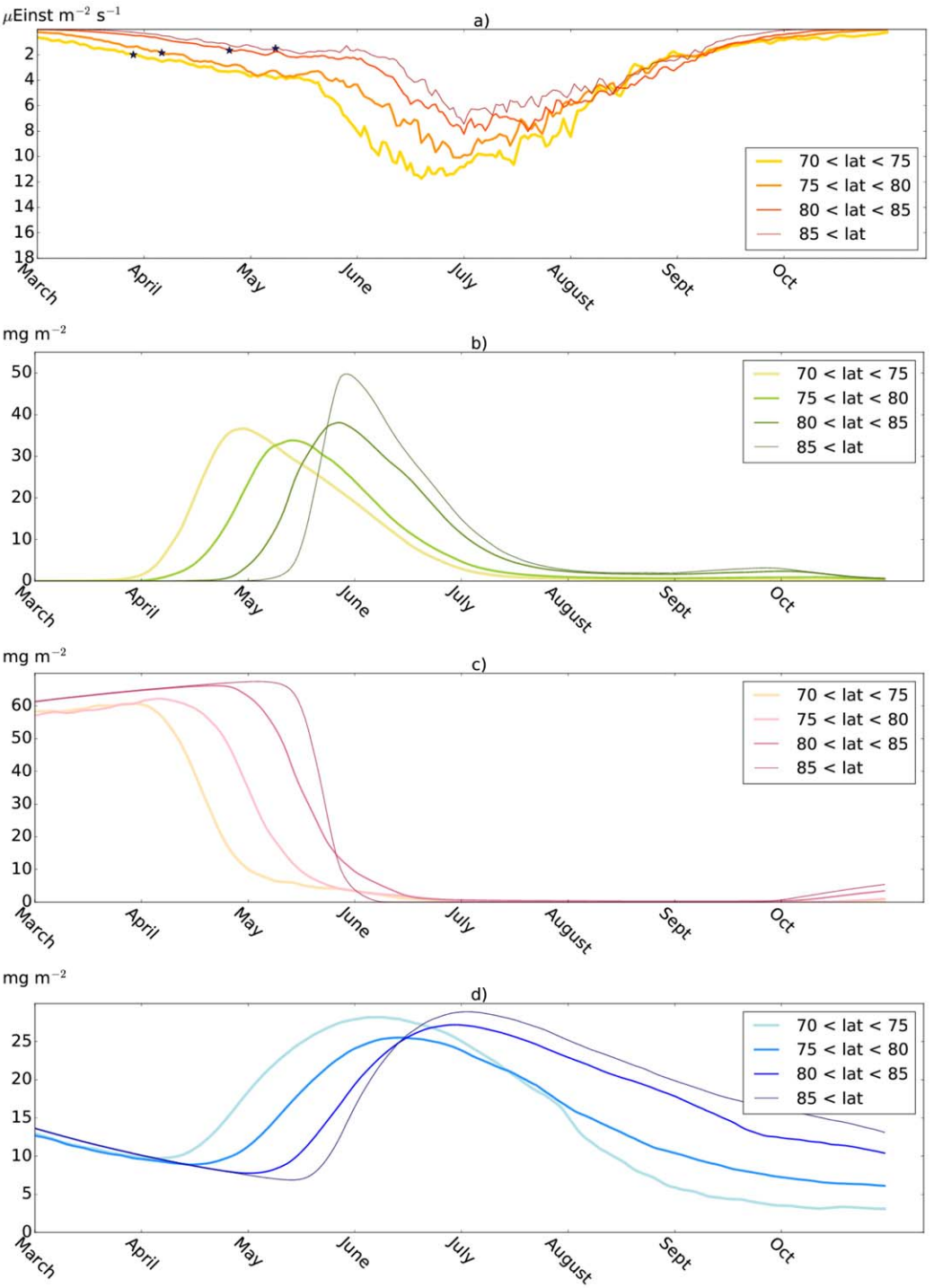

Figure 6. Model simulation between March and November for: (a) under-ice light (positive downward) for the grid-averaged sea ice, (b) sea-ice algal bloom, (c) nutrient concentration, and (d) detritus concentration. Results are presented as averages over four latitudinal sectors as shown in Figure 2. The stars in Figure 6a identify the onset of algal bloom in each latitudinal band (values are listed in Table 5).

(equation (14)) varies between a minimum of 0.1 cm in the northern regions (particularly north of 85°N and in the Nansen Basin) and a maximum of 1.5 cm ice loss in the marginal areas (Figure 10). Particularly high values are found in the East Siberian Sea, north of the Laptev Sea and in the Canadian Archipelago. North of the Svalbard islands and within a triangle, delineated by the 10°W and the 90°E meridians pointing toward the North Pole, the algae-induced melt values are low.

Table 5. Key Numbers to Characterize and Compare the Numerical Experiments: Day of Bloom Onset Defined as the Day From Beginning of January When the Algae Start Growing Exponentially, Inferred From the Slope of the Curves in Figure 6b; Corresponding Value of PAR Considered as the Threshold for Algal Bloom; Day When the Peak of Biomass is Reached; and Value of Maximum Biomass[a]

Ice Type	Sector	Bloom Onset (day)	Light (μEinst m^{-2} s^{-1})	Day of Max Biomass (day)	Maximum Biomass (mg chl *a* m^{-2})
G-Ave	70°N < lat <75°N	87	2	118	37
	75°N < lat <80°N	95	1.84	132	34
	80°N < lat <85°N	114	1.65	146	38
	85°N < lat	127	1.49	148	50
Lev	70°N < lat <75°N	92	1.79	128	37
	75°N < lat <80°N	102	1.78	139	33
	80°N < lat <85°N	121	1.40	154	34
	85°N < lat	134	1.56	157	48
Rid	70°N < lat <75°N	118	1.13	161	14
	75°N < lat <80°N	123	1.20	151	10
	80°N < lat <85°N	138	0.96	166	11
	85°N < lat	149	0.73	175	8

[a]Values are computed for the grid-averaged ice (G-Ave), for level ice (Lev), and for ridged ice (Rid). Results are divided in four different sectors according to latitude (see also Figure 2).

3.3. Distinction Between Level Ice and Ridged Ice

According to equations (2) and (3), we divide the ice into level ice and ridged ice. In Figure 11, we show the ridge density (number of ridges per km), the total thickness of ridged ice, and differences in ice and snow thickness between level ice and the grid-averaged ice for May. This is an illustrative example because in May the algal bloom for the grid-averaged ice just started at higher latitudes. Moreover, in May, there is still snow on the ice. The ridge density (Figure 11a) is high, with values up to 20 ridges per kilometer in the western part of the Nansen Basin and particularly along the coast of Svalbard islands and Severnaya Zemlya islands. Lower values (<10 ridges per kilometer) are mainly found in the Beaufort Sea, Laptev Sea, and East Siberian Sea. The thickness of the ridged ice (Figure 11b) remains between 4 and 6 m in almost the entire Arctic Ocean, values higher than 10 m are found mainly in the Lincoln Sea and along the northern coast of Greenland. Both ice and snow thickness have large variations in the longitudinal direction in the sector between 100°W and 100°E, where also the number of ridges is higher.

We analyze algal bloom in relation to the under-ice light field for both level ice and ridged ice in the different latitudinal sectors (Figure 12). In Table 5, we list (as done for the grid-averaged ice) day of bloom onset, the corresponding value of PAR, and the day and value of maximum chl *a* concentration. For level ice, day of bloom onset and day of maximum biomass are delayed by 5–10 days compared to the grid-averaged ice (see Table 5), but they still occur 20 days (bloom onset) and 19 days (maximum biomass) earlier than in ridged ice. Maximal biomass values for level ice are very close to the grid-averaged ice values with differences no larger than 4 mg chl *a* m^{-2}.

The light field under ridges is much weaker compared to the level ice and grid-averaged ice (Figures 6 and 12). Nevertheless, a minimum light threshold value of 0.36 μEinst m^{-2} s^{-1} [*Mock and Gradinger*, 1999] for algal growth is reached, and a small algal bloom develops. The bloom under ridged ice in each latitudinal sector starts later than for the grid-averaged ice. In the two southernmost sectors, the delay is up to 30 days, whereas north of 80°N the delay is 20 days. The maximum is also reached later with a delay of 20–40 days compared to grid-averaged sea ice. Moreover, the southernmost band shows a slower growth with a maximum biomass reached 10 days later than in the band 75°N < lat <80°N. The values of maximum biomass are half of the grid-averaged and level ice values. In particular, the maximum biomass under ridged ice in the latitudinal sector north of 85°N is smaller than the values of maximum biomass in the other sectors, opposite to what happens in level ice and grid-averaged ice.

In both level ice and ridged ice, nitrate increases during the first months of the year reaching values around 70 mg m^{-2} (Figure 13). Between mid-April and mid-June, the nutrient concentrations start to decrease. Toward the beginning of July, the level ice is nutrient depleted in all the four latitudinal sectors. Under the ridged ice, nitrate concentrations are never exhausted.

In March and April, the total algae biomass (i.e., the chl *a* concentration integrated over the area of the grid cell and weighted by sea-ice concentration) of level ice is always larger than the total algal biomass of grid-averaged ice (Figure 14 shows the ratio of the two). In May, the total biomass ratio of level to grid-averaged ice is no longer larger than 1 everywhere, but only in the latitudinal band 70°N < lat <75°N and in part of the band 75°N < lat <80°N. For latitudes higher than 80°N, the ratio is always smaller than 1. In June, there is more biomass in the level ice than in the grid-averaged ice in all regions.

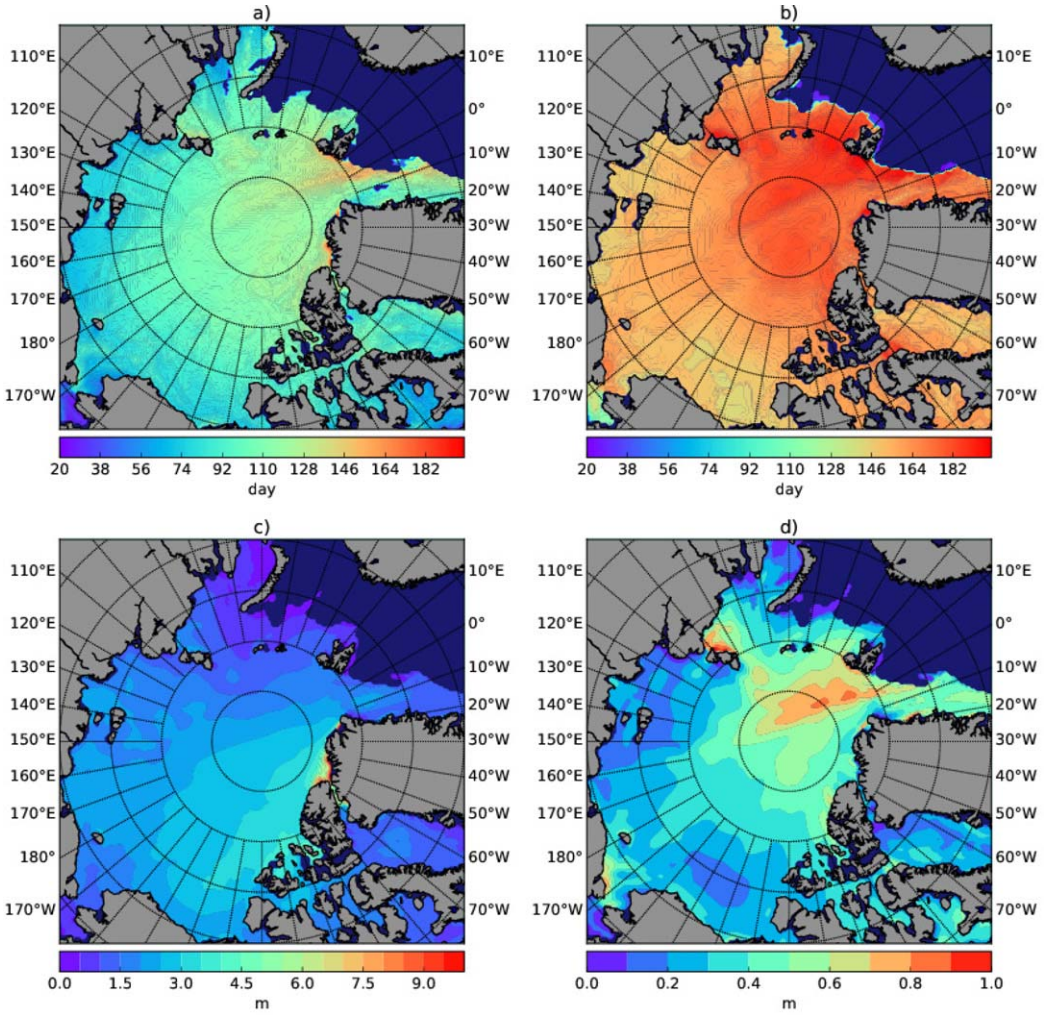

Figure 7. Maps for the Arctic showing (a) bloom onset as the day from the beginning of January, (b) complete snow melt ($H_s = 0$) as the day from the beginning of January, (c) ice thickness at the day of bloom onset, and (d) snow thickness at the day of bloom onset.

The ratio of ridged-ice algae to grid-averaged ice algae is almost always small, about 0.05–0.1 (5%–10%) in June and July (Figure 15), except for a band in July extending from the Beaufort Sea and Bering Strait to the Fram Strait with values up to 0.5 (50%).

4. Discussion

4.1. Performance of SIMBA

The simulated spatial pattern of sea-ice algae concentrations at the end of summer resembles the pattern obtained from observations (BLROV). There is a belt of lower chl *a* concentration extending toward the sea ice edge within the eastern sector (Figure 4). In this area, the model reproduces the values from observations (Table 4). The algae concentration increases toward the central Arctic. Here the modeled mean ice algae concentration and field measurements are different. North of 85°N, however, observations are in the range of modeled values. The latitudinal pattern of algae concentrations increasing from south to north was already observed in July–August 1994 [*Gosselin et al.*, 1997]. In particular, they report values of bottom sea-ice algal chl *a* concentrations (3–14 mg chl *a* m^{-2}) in the area close to the North Pole, which are 3 times higher than in the latitudinal bands south of 70°N. North of 85°N, particularly in the Eastern sector, model results agree with summer values of 1–7 mg chl *a* m^{-2} in 1991 [*Gradinger*, 1999]. In agreement with model results, low values of chl *a* concentrations ($<$1 mg chl *a* m^{-2}) were also observed at the end of summer during a 1993 study in the Laptev Sea and north of Svalbard [*Gradinger and Zhang*, 1997], in 1994 and 1995 in

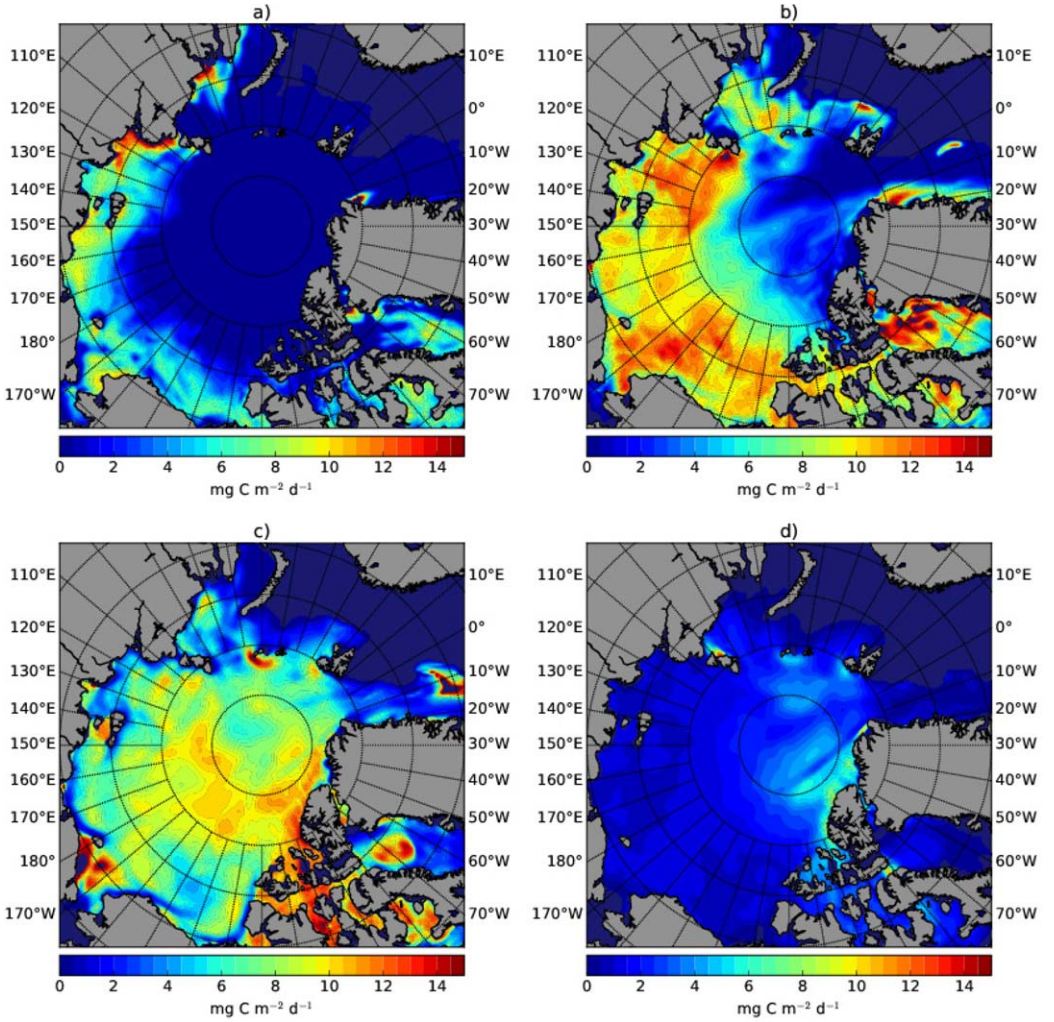

Figure 8. Maps of monthly averaged sea-ice algae NPP for (a) April, (b) May, (c) June, and (d) July 2012.

the Fram Strait and Greenland Sea [*Gradinger et al*., 1999; *Werner and Gradinger*, 2002], in 1998 in the Chukchi plateau [*Melnikov et al*., 2002], in 2002 in the Fram Strait [*Schünemann and Werner*, 2005], in 2002 and 2003 in the Beaufort Gyre [*Gradinger et al*., 2005], and in 2005 in the Chukchi/Beaufort Sea [*Gradinger et al*., 2010]. The only two studies [*Lange et al*., 2015, 2017] of sea-ice algae concentration in the Lincoln Sea are from the spring season. *Lange et al*. [2015, 2017] show mean values of sea-ice algae concentration for spring 2012 below 2 mg chl *a* m^{-2}, where the model estimates a mean concentration of 1.93 mg chl *a* m^{-2}. Note that all studies cited above focus mainly on thicker ice, in particular, we consider for our comparison only literature values for ice thicker than 1.5 m to reduce the risk of measurements biased toward the thinner sea-ice classes.

What might be interpreted as a merely latitudinal dependency from observations alone, has a different interpretation from our model results. Here the algae concentration follows a latitudinal pattern on the Eastern side (~20°E to 180°E, see Figure 4), but it also depends strongly on thickness, which increases closer to the coast within the western sector. Analyzing the total summer melt (Figure 5) we see a very similar pattern at the end of summer, even though the correlation coefficients are small ($r < 0.2$). In particular, the very thick ice in the Lincoln Sea has lower algal loss due to lower melt rates in this region [*Dupont*, 2012].

The algal bloom is initiated after PAR exceeds a lower limit (Figure 6) [see also *Horner and Schrader*, 1982; *Gosselin et al*., 1986; *Mock and Gradinger*, 1999; *Lange et al*., 2015]. The spatial distribution of the bloom onset (Figure 7) suggests that factors other than latitude (i.e., incoming radiation, albedo, ice thickness and

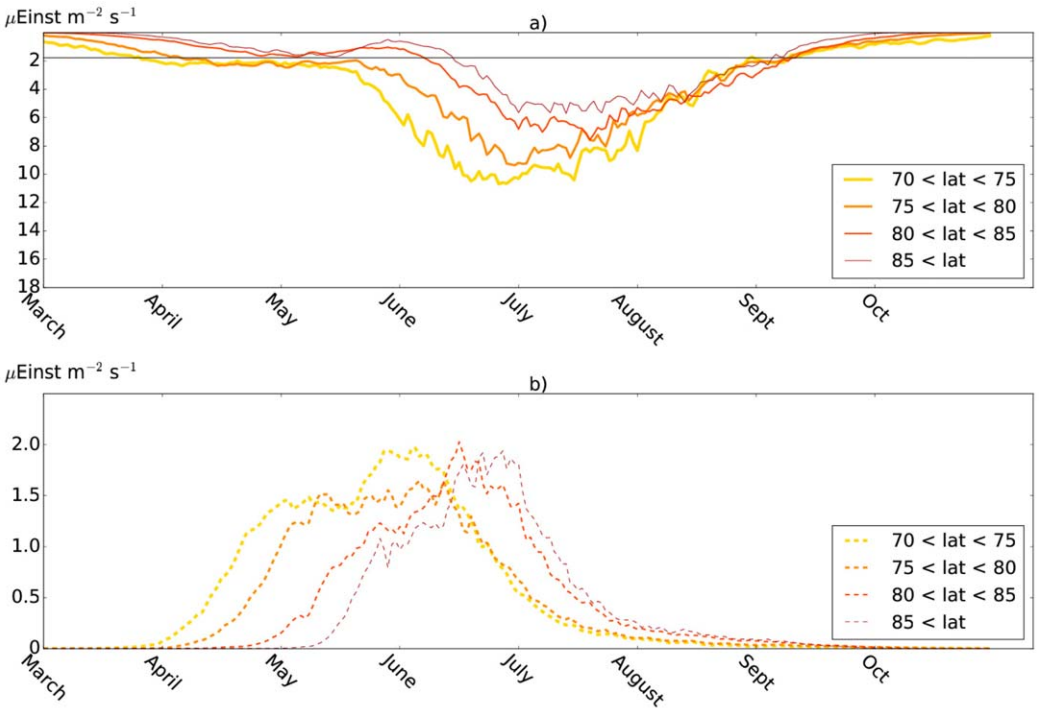

Figure 9. Plots of (a) under-ice light when the shading effect due to sea-ice algae is considered, and (b) differences between under-ice light computed without algae shading (Figure 6a) and under-ice light computed considering the shading effect due to algae. The horizontal gray line in Figure 9a at 1.78 μEinst m^{-2} s^{-1} represents the limit for algal bloom as average of values indicated by stars in Figure 6a.

snow thickness) affect the spatial distribution. It is, however, very difficult to decouple the effects of these single variables. For example, the late bloom in the Lincoln Sea can be explained by the large sea-ice thickness values whereas the delay in the Kara Sea and Fram Strait is caused by the thicker snow cover. Correlations of day of bloom onset with day of snow melt ($r = 0.19$) and with ice thickness ($r = 0.22$) are weak but significant. A moderate correlation ($r = 0.57$) is found with the snow thickness distribution. Such low correlation values are caused by the large area considered and the large scale of variability of all variables controlling ice algal growth. The correlation should be investigated at smaller scales because sea-ice algae biomass in different regions of the Arctic can have substantially different relationships with the physical sea ice environment.

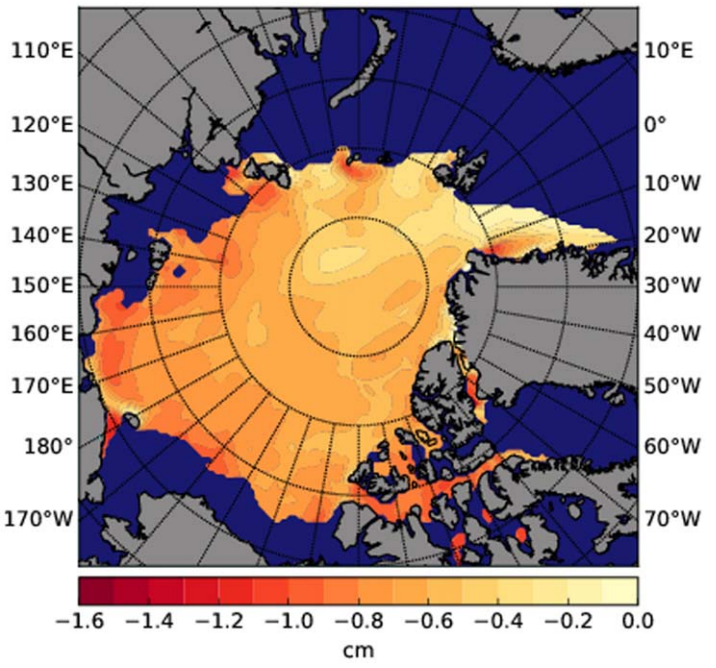

Figure 10. Integrated summer basal ice melt over the period April to September 2012 caused by heat released by sea-ice algae.

The maximum chl *a* concentration is also reached later in the higher latitude regions. We compare our results with what is shown in *Leu et al.* [2015]. We look at the curves for the

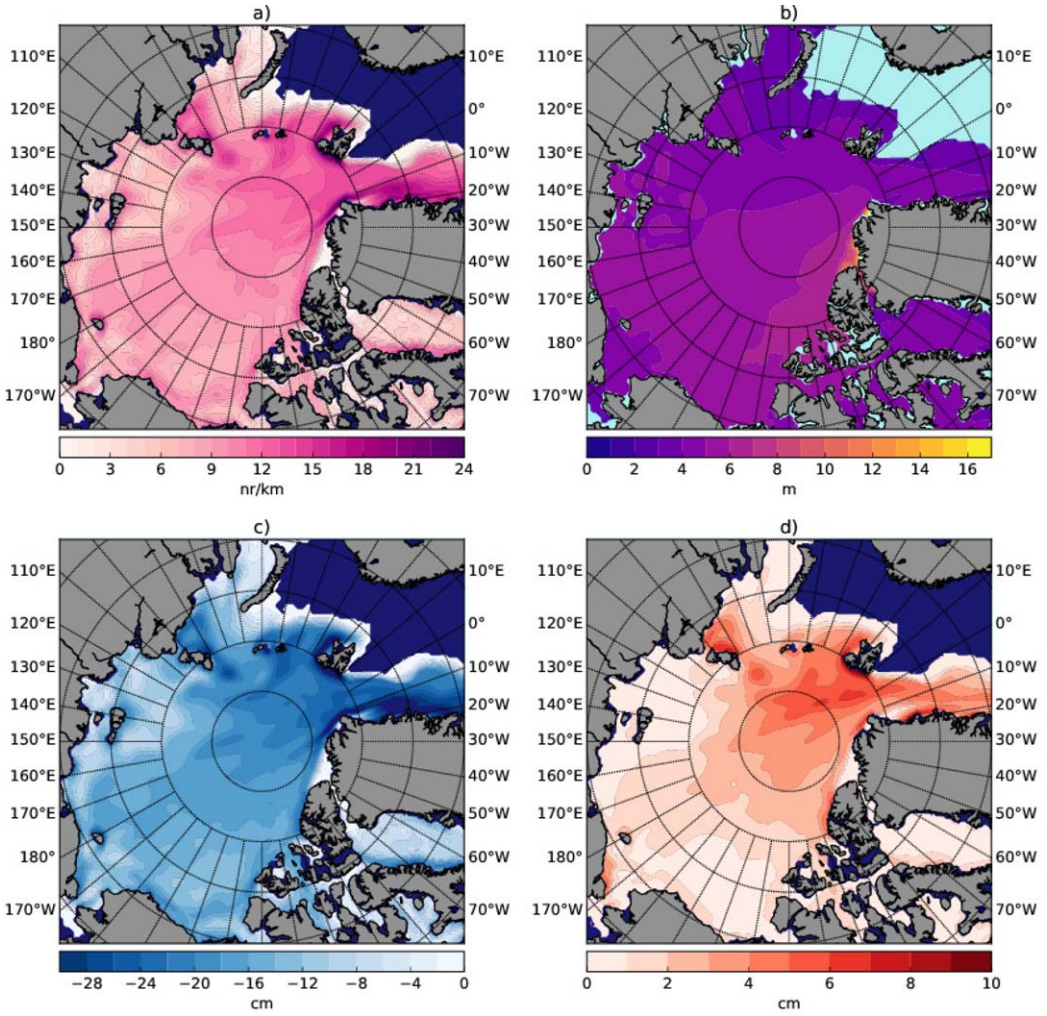

Figure 11. Maps of May averages for: (a) ridge density, (b) thickness of ridged ice, (c) differences in ice thickness between level ice and grid-averaged ice, and (d) snow thickness differences between level ice and the grid-averaged ice.

stations in the two regions of interest and compare the day and value of maximum with our results. From *Leu et al*. [2015], we infer a day of maximum biomass of 138 and 146 for the two regions 70°N < lat <75°N and 75°N < lat <80°N with maxima of ∼14.5 and ∼22.5 mg chl *a* m^{-2}, respectively. Our results for day of maximum biomass are 20 and 14 days earlier, respectively (Table 5), and show a higher maximum value of chl *a* concentrations (more than double in the southernmost latitudinal band). Since we discard a latitudinal effect in the comparison, further investigation to asses the cause of the earlier modeled day of maximum biomass should be addressed (but not performed in the present study). We may speculate that the spatial coverage of observations is heavily biased toward coastal regions and landfast sea ice, which may have different nutrient regimes and dynamic sea-ice processes. Moreover, the simplified nutrient initialization used in the present study can lead to overestimating the maximum biomass values (see section 4.2).

4.2. Effects of Different Initial Conditions

We use the algal bloom as a key process to compare different scenarios listed in Table 3 and to investigate the effect of different initial conditions. Between scenarios R2, R4, R6, and R8, the differences in bloom onset are only ±2 days. The largest difference between these scenarios is the maximum biomass reached during the bloom. Nitrate availability in winter and spring determines the total primary production in the late spring so that highest biomass peaks are reached in runs with higher initial nutrient concentration. This shows the key role of nutrient concentrations in winter and thus the importance of having observations

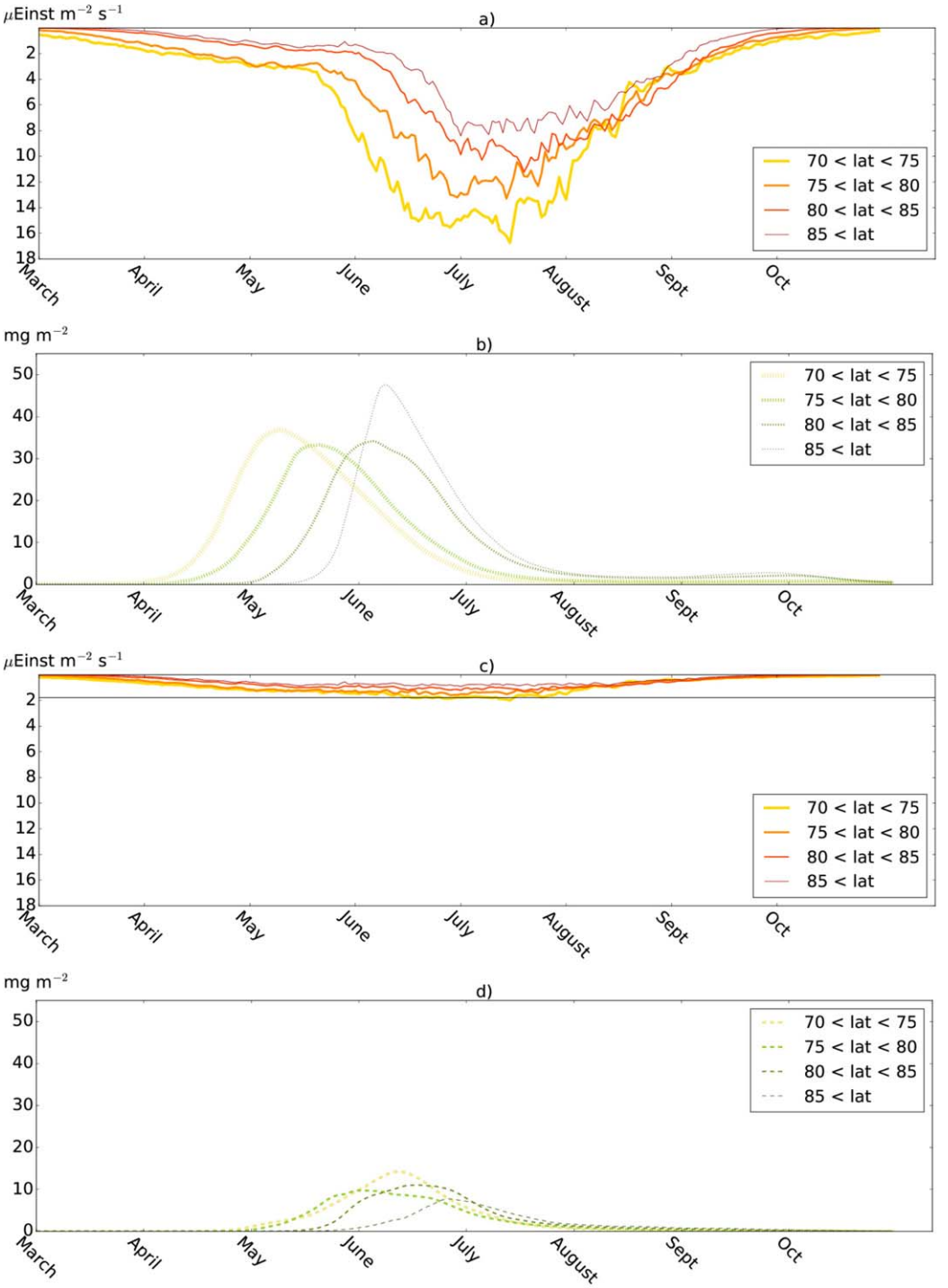

Figure 12. Level ice: (a) under-ice light and (b) algae evolution. Ridged ice: (c) under-ice light and (d) algae evolution. The horizontal gray line in Figure 12c represents the limit value for PAR of 1.78 μEinst m^{-2} s^{-1} inferred by Figure 6. Quantities are averaged over the four latitudinal sectors shown in Figure 2.

collected before the algal bloom. Of particular interest is scenario R0, which has the lowest maximum biomass, but also shows an earlier bloom period (40 days earlier). Furthermore, the decay is slower for R0 compared to other scenarios, so the minimum is reached between August and September, which is consistent with other runs. This means that the conditions at the end of summer are similar for all scenarios, as can be seen in Table 3.

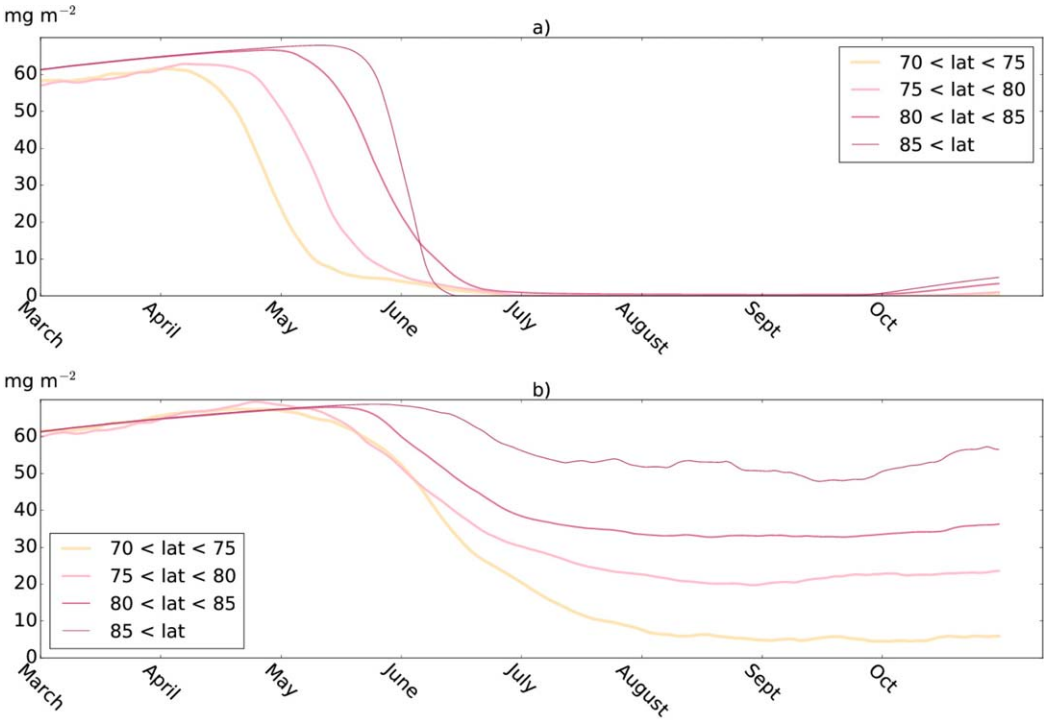

Figure 13. Nutrient evolution for (a) level ice, and (b) ridged ice in the four latitudinal sectors shown in Figure 2.

4.3. Effects Caused by Ice Algae on Ice and Ocean

Ice algae can have an influence on both ocean and sea ice. The shading created by sea-ice algae can delay the under-ice phytoplankton bloom, thus further extending the thriving window for sympagic and pelagic grazers [*Jin et al*., 2012; *Tremblay et al*., 2008]. Our results show that the shading effect due to sea-ice algae differs according to the different latitudinal sectors. Between 70°N and 80°N, ice algae keep the light level around the mean threshold so that some growth is possible for under-ice phytoplankton. North of 80°N, the light level is under the threshold value due to the shading effect, thus under-ice phytoplankton bloom may be delayed by up to ∼40 days, if not completely prevented as shown by *Dupont* [2012]. Such shading effects may add to the shading already caused by ice and snow on the ocean surface, thus further delaying the phytoplankton blooms under the ice compared to the blooms in open water [*Arrigo et al*., 2012]. However, the presence of sea-ice algae can have other effects on phytoplankton growth. Such effects include, e.g., uptake and remineralization of nutrients by sea-ice algae, but their investigation requires coupling to an ocean biogeochemical model. Thus, the results presented here for the effects of ice algae on under-ice phytoplankton blooms should be corroborated with a coupled ice algae-phytoplankton model.

The ice algae-induced melt, integrated from April to August, ranges from 0 to 2 cm and agrees with previous studies [*Zeebe et al*., 1996]. Ice algae-induced melt is much smaller than the range of variability of the physically induced melt (0–1.5 m) and thus negligible for the physical system. Nevertheless, this positive feedback mechanisms can have measurable effects in long-term simulations. Moreover, the total ice algae-induced melt can be important for the algae layer, which could be eroded by the melt induced by the ice algae.

4.4. Level Ice and Ridged Ice

After dividing sea ice into level ice and ridged ice based on the deformation energy and sail density, resulting level ice is thinner than the grid-averaged ice, but it has a thicker snow cover (Figure 11). These differences are reflected in light transmission and algae phenology. In the presence of snow, there is less light under level ice than under the grid-averaged ice, but after all snow is melted, there is more light under level ice because of thinner ice. Since the amount of nutrients is the same, the maximum chl *a* concentration is very similar, mostly because the system is determined by initial conditions for nutrients (section 4.2 and Table 5). Nevertheless, the presence of thicker snow has an important influence on the timing of algal

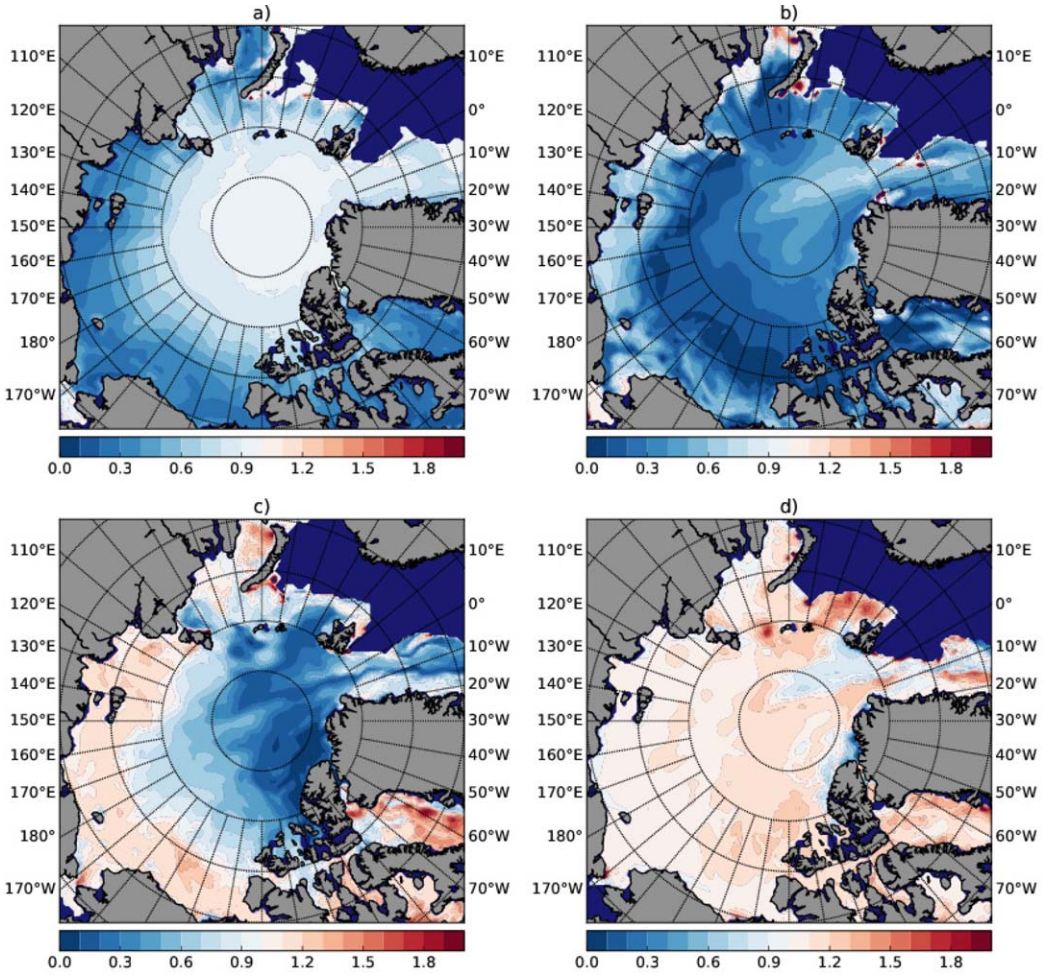

Figure 14. Ratio between grid integrated level-ice algae and grid-averaged ice algae in (a) March, (b) April, (c) May, and (d) June 2012.

growth. Figure 14 shows that in April there are more algae associated with the grid-averaged ice. This ratio changes in May, when in the Marginal Ice Zone the level-ice algae are close to the maximum of the bloom, whereas the grid-averaged ice algae start to decay. In June, algae associated to the grid-averaged sea ice

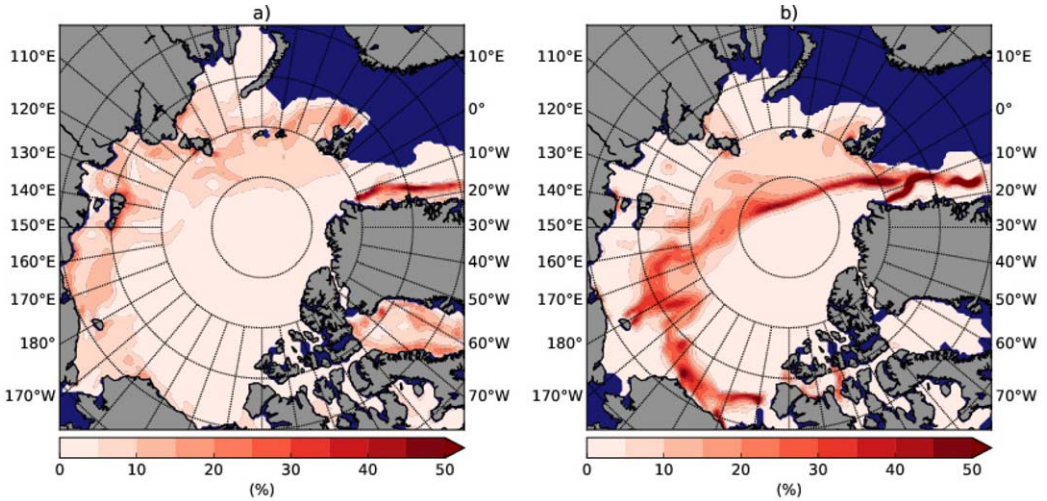

Figure 15. Grid integrated ridged-ice algal biomass as percent of grid-averaged ice algae for (a) June and (b) July.

are already decreasing whereas the amount of biomass associated with level ice is still high. Thus, changes in the snow cover, rather than in ice thickness, have a large effect on the timing of the algal bloom.

Ridges create a very special environment for ice algae [*Kuparinen et al*., 2007; *Vancoppenolle et al*., 2013]. As such, they show a pattern for both physical factors and algal growth different from level ice and grid-averaged ice. The ridge-associated algae can constitute more than 50% of the total algae that grow under the grid-averaged ice (Figure 15). Due to the specific light conditions, the bloom under ridged ice appears later in the season than for grid-averaged ice or level ice, thus it can provide an extra source of carbon toward the end of the feeding season when other food sources are already depleted. We stress that our parameterization does not provide an accurate representation of the structural and geometrical properties of ridges. Potential effects along the ridge edges, where ridges are thinner and might let more light pass through due to horizontal scattering, are not included in this work. Moreover, ridges can incorporate water pockets during formation, which could represent a nutrient reservoir for algae. Finally, scattering and absorption processes in ridges are not yet parameterized.

The distinction between level and ridged ice classes shows that with the grid-averaged ice only, it may not be possible to accurately represent the actual timing of algal growth and bloom. Based on our modeling results, in combination with floe-scale observations (BLROV) we recommend that different ice classes should be considered when the aim is to model algae content and evolution.

5. Conclusions and Outlook

A new Arctic-wide sea-ice algal model coupled to a sea-ice–ocean general circulation model helps interpreting observations of ice algal biomass. In spite of its simplicity, the new model reproduces part of the observed distributions of biomass, in particular, the latitudinal pattern in an eastern sector south of 80°N. In other areas, snow and ice thickness affect light availability and thus algal growth in a complicated manner. In this situation, the interpretation of observations is difficult, because often the available data sets do not provide all the pieces of information required to attribute the phenology of sea-ice algae to physical constraints.

Ice-algae phenology is driven by different physical factors that vary with season and region. Ice-algal blooms are delayed with latitude (i.e., light) and affected by snow and ice thickness. The bloom peak values depend on initial conditions, especially of nutrients. In all cases, nutrient limitation terminates the bloom and by the end of summer the algae concentration pattern resembles that of the basal melt. A better spatial and temporal coverage of observations, ideally during the key transition periods between the onset of the bloom until the end of summer, is required to validate the accuracy of these numerical model experiments for the entire period.

The shading effect due to an algae layer and the increased melting due to energy released by algae as heat are two mechanisms that feed back into the physical sea-ice and ocean system. The shading effect is not important south of 80°N, but north of 80°N it can delay the under-ice phytoplankton bloom by up to 40 days. The release of heat by ice algae can contribute to an overall annual sea ice melt of up to 2 cm, much smaller than the total melt due to physical processes.

The algal bloom and decay are functions of the physical properties of level and ridged ice. Level ice is thinner than grid-cell averaged ice, but the redistribution of snow results in more snow on level ice. This extra snow delays the onset of the algal bloom under level ice. Ridged ice can host algae communities that grow and support primary production when a minimum value of under-ice light is reached in summer. Thus, they represent an additional food source for sympagic and pelagic species during the end of summer when other food resources are limited. Our results show that different sea-ice classes might be useful in properly representing sea-ice algae spatial distribution and phenology.

The model is at an early stage of development and is lacking the representation of some important processes. In particular, the exchange of nutrients with the underlying ocean is an important term to sustain the growth and survival of bottom sea-ice algae after nutrients that have been captured within the sea-ice matrix at the time of freezing are depleted. For multiyear simulations, which allow to asses interannual changes in sea-ice algae concentrations, the initialization of nutrients and ice algae at ice formation need to

be parameterized. The model could further be improved by coupling the biogeochemical processes at the bottom of sea ice to those within the upper ocean, that is to an ocean-biogeochemical module.

Acknowledgments
This study is part of the Helmholtz Association Young Investigators Group *Iceflux*: Ice-ecosystem carbon flux in polar oceans (VH-NG-800). We sincerely thank two anonymous reviewers for the constructive comments on previous versions of the present manuscript. The general MITgcm code is available at http://mitgcm.org/. The code for SIMBA and the routines used for the analysis are available on PANGEA: https://doi.org/10.1594/PANGAEA.879783.

References

Arrigo, K. R., and G. L. van Dijken (2011), Secular trends in Arctic Ocean net primary production, *J. Geophys. Res.*, *116*, C09011, doi:10.1029/2011JC007151.

Arrigo, K. R., J. N. Kremer, and C. W. Sullivan (1993), A simulated Antarctic fast ice ecosystem, *J. Geophys. Res.*, *98*(C4), 6929–6946, doi:10.1029/93JC00141.

Arrigo, K. R., D. L. Worthen, M. P. Lizotte, P. Dixon, and G. Dieckmann (1997), Primary production in Antarctic sea ice, *Science*, *276*(5311), 394–397, doi:10.1126/science.276.5311.394.

Arrigo, K. R., et al. (2012), Massive phytoplankton blooms under Arctic sea ice, *Science*, *336*(6087), 1408–1408, doi:10.1126/science.1215065.

Belém, A. L. (2002), Modeling physical and biological processes in Antarctic sea ice, PhD thesis, Univ. of Bremen, Bremen, Germany.

Castellani, G. (2014), Momentum exchange between atmosphere, sea ice and ocean, PhD thesis, Jacobs Univ., Bremen, Germany.

Castellani, G., C. Lüpkes, S. Hendricks, and R. Gerdes (2014), Variability of Arctic sea ice topography and its impact on the atmospheric surface drag, *J. Geophys. Res. Oceans*, *119*, 6743–6762, doi:10.1002/2013JC009,712.

Castro-Morales, K., F. Kauker, M. Losch, S. Hendricks, K. Riemann-Campe, and R. Gerdes (2014), Sensitivity of simulated Arctic sea ice to realistic ice thickness distributions and snow parameterizations, *J. Geophys. Res. Oceans*, *119*, 559–571, doi:10.1002/2013JC009,342.

Comiso, J. C. (2012), Large decadal decline of the Arctic multiyear ice cover, *J. Clim.*, *25*(4), 1176–1193, doi:10.1175/JCLI-D-11-00113.1.

Cota, G. F., S. J. Prinsenberg, E. B. Bennett, J. W. Loder, M. R. Lewis, J. L. Anning, N. H. F. Watson, and L. R. Harris (1987), Nutrient fluxes during extended blooms of Arctic ice algae, *J. Geophys. Res.*, *92*(C2), 1951–1962, doi:10.1029/JC092iC02p01951.

Deal, C., M. Jin, S. Elliott, E. Hunke, M. Maltrud, and N. Jeffery (2011), Large-scale modeling of primary production and ice algal biomass within arctic sea ice in 1992, *J. Geophys. Res.*, *116*, C07004, doi:10.1029/2010JC006409.

Dupont, F. (2012), Impact of sea-ice biology on overall primary production in a biophysical model of the pan-Arctic Ocean, *J. Geophys. Res.*, *117*, C00D17, doi:10.1029/2011JC006983.

Fernández-Méndez, M., C. Katlein, B. Rabe, M. Nicolaus, I. Peeken, K. Bakker, H. Flores, and A. Boetius (2015), Photosynthetic production in the central Arctic Ocean during the record sea-ice minimum in 2012, *Biogeosciences*, *12*(11), 3525–3549, doi:10.5194/bg-12-3525-2015.

Fernández-Méndez, M., K. A. Turk-Kubo, P. L. Buttigieg, J. Z. Rapp, T. Krumpen, J. P. Zehr, and A. Boetius (2016), Diazotroph diversity in the sea ice, melt ponds, and surface waters of the Eurasian basin of the Central Arctic Ocean, *Frontiers Microbiol.*, *7*(1884), 1–18, doi:10.3389/fmicb.2016.01884.

Frouin, R., and R. T. Pinker (1995), Estimating photosynthetically active radiation (PAR) at the Earth's surface from satellite observations, *Remote Sens. Environ.*, *51*, 98–107.

Gosselin, M., L. Legendre, J.-C. Therriault, S. Demers, and M. Rochet (1986), Physical control of the horizontal parchiness of sea-ice microalgae, *Mar. Ecol. Prog. Ser.*, *29*, 289–298.

Gosselin, M., M. Levasseur, P. A. Wheeler, R. A. Horner, and B. C. Booth (1997), New measurements of phytoplankton and ice algal production in the Arctic Ocean, *Deep Sea Res., Part II*, *44*(8), 1623–1644.

Gradinger, R. (1999), Vertical fine structure of the biomass and composition of algal communities in Arctic pack ice, *Mar. Biol.*, *133*(4), 745–754, doi:10.1007/s002270050516.

Gradinger, R., and Q. Zhang (1997), Vertical distribution of bacteria in Arctic sea ice from the Barents and Laptev Seas, *Polar Biol.*, *17*(5), 448–454, doi:10.1007/s003000050139.

Gradinger, R., C. Friedrich, and M. Spindler (1999), Abundance, biomass and composition of the sea ice biota of the Greenland Sea pack ice, *Deep Sea Res., Part II*, *46*(6–7), 1457–1472, doi:10.1016/S0967-0645(99)00030-2.

Gradinger, R., B. A. Bluhm, and K. Iken (2010), Arctic sea-ice ridges—Safe heavens for sea-ice fauna during periods of extreme ice melt?, *Deep Sea Res., Part II*, *57*(1–2), 86–95, doi:10.1016/j.dsr2.2009.08.008.

Gradinger, R., K. Meiners, G. Plumley, Q. Zhang, and B. A. Bluhm (2005), Abundance and composition of the sea-ice meiofauna in off-shore pack ice of the Beaufort Gyre in summer 2002 and 2003, *Polar Biol.*, *28*(3), 171–181, doi:10.1007/s00300-004-0674-5.

Grenfell, T. C., and G. A. Maykut (1977), The optical properties of ice and snow in the Arctic basin, *J. Glaciol.*, *18*(80), 445–463.

Grossi, S., S. Kottmeier, R. Moe, G. Taylor, and C. W. Sullivan (1987), Sea ice microbial communities. Growth and primary production in bottom ice under graded snow cover, *Mar. Ecol. Prog. Ser.*, *35*, 153–164.

Haas, C., A. Pfaffling, S. Hendricks, L. Rabenstein, J.-L. Etienne, and I. Rigor (2008), Reduced ice thickness in Arctic Transpolar Drift favors rapid ice retreat, *Geophys. Res. Lett.*, *35*, L17501, doi:10.1029/2008GL034,457.

Hibler, W. D. III (1979), A dynamic thermodynamic sea ice model, *J. Phys. Oceanogr.*, *9*, 815–846.

Hibler, W. D. III (1980), Modeling a variable thickness sea ice cover, *Mon. Weather Rev.*, *108*, 1943–1973.

Hibler, W. D. III (1984), The role of sea ice dynamics in modeling CO_2 increases, in *Climate Processes and Climate Sensitivity*, edited by J. E. Hansen and T. Takahashi, pp. 238–253, AGU, Washington, D. C., doi:10.1029/GM029p0238.

Horner, R. A., and G. C. Schrader (1982), Relative contributions of ice algae, phytoplankton, and benthic microalgae to primary production in nearshore regions of the Beaufort Sea, *ARCTIC*, *35*(4), 485–503.

Iacozza, J., and D. G. Barber (1999), An examination of the distribution of snow on sea-ice, *Atmo. Ocean*, *37*(1), 21–51.

Ivanova, N., O. M. Johannessen, L. T. Pedersen, IEEE-Members, and R. T. Tonboe (2014), Retrieval of Arctic Sea ice parameters by satellite passive microwave sensors: A comparison of eleven sea ice concentration algorithms, *IEEE Trans. Geosci. Remote Sens.*, *52*(11), 7233–7246.

Ji, R., M. Jin, and Ø. Varpe (2013), Sea ice phenology and timing of primary production pulses in the Arctic Ocean, *Global Change Biol.*, *19*(3), 734–741, doi:10.1111/gcb.12074.

Jin, M., J. C. Deal, J. Wang, K.-H. Shin, N. Tanaka, T. E. Whitledge, S. H. Lee, and R. R. Gradinger (2006), Controls of the landfast ice-ocean ecosystem offshore Barrow, Alaska, *Ann. Glaciol.*, *44*, 63–72.

Jin, M., C. Deal, S. H. Lee, S. Elliott, E. Hunke, M. Maltrud, and N. Jeffery (2012), Investigation of Arctic sea ice and ocean primary production for the period 1992–2007 using a 3-D global ice–ocean ecosystem model, *Deep Sea Res., Part II*, *81–84*, 28–35.

Kirk, J. T. O. (1983), *Light and Photosynthesis in Aquatic Ecosystems*, 401 pp., Cambridge Univ. Press, New York.

Kohlbach, D., M. Graeve, B. A. Lange, C. David, I. Peeken, and H. Flores (2016), The importance of ice algae-produced carbon in the central Arctic Ocean ecosystem: Food web relationships revealed by lipid and stable isotope analyses, *Limnol. Oceanogr.*, *61*(6), 2027–2044, doi:10.1002/lno.10351.

Kohlbach, D., F. L. Schaafsma, M. Graeve, B. Lebreton, B. A. Lange, C. David, M. Vortkamp, and H. Flores (2017), Strong linkage of polar cod (*Boreogadus saida*) to sea ice algae-produced carbon: Evidence from stomach content, fatty acid and stable isotope analyses, *Prog. Oceanogr.*, *152*, 62–74, doi:10.1016/j.pocean.2017.02.003.

Kuparinen, J., et al. (2007), Role of sea-ice biota in nutrient and organic material cycles in the northern Baltic Sea, *Ambio*, *36*(2–3), 149–154.

Kwok, R., and D. A. Rothrock (2009), Decline in Arctic sea ice thickness from submarine and ICEsat records, *Geophys. Res. Lett.*, *36*, L15501, doi:10.1029/2009GL039035.

Kwok, R., G. F. Cunningham, M. Wensnahan, I. Rigor, H. J. Zwally, and D. Yi (2009), Thinning and volume loss of the Arctic Ocean sea ice cover: 2003–2008, *J. Geophys. Res.*, *114*, C07005, doi:10.1029/2009JC005312.

Lange, B. A. (2016), Spatial variability of Arctic sea ice algae, PhD thesis, Univ. of Hamburg, Hamburg, Germany. [Available at http://ediss.sub.uni-hamburg.de/volltexte/2017/8460.]

Lange, B. A., C. Michel, J. F. Beckers, J. A. Casey, H. Flores, I. Hatam, G. Meisterhans, A. Niemi, and C. Haas (2015), Comparing springtime ice-algal chlorophyll a and physical properties of multi-year and first-year sea ice from the Lincoln Sea, *PLoS ONE*, *10*(4), e0122,418, doi:10.1371/journal.pone.0122418.

Lange, B. A., C. Katlein, M. Nicolaus, I. Peeken, and H. Flores (2016), Sea ice algae chlorophyll *a* concentrations derived from under-ice spectral radiation profiling platforms, *J. Geophys. Res. Oceans*, *121*, 8511–8534, doi:10.1002/2016JC011991.

Lange, B. A., et al. (2017), Pan-Arctic sea ice-algal chl *a* biomass and suitable habitat are largely underestimated for multiyear ice, *Global Change Biol.*, 1–17, doi:10.1111/gcb.13742, in press.

Lavoie, D., K. Denman, and C. Michel (2005), Modeling ice algal growth and decline in a seasonally ice-covered region of the Arctic (Resolute Passage, Canadian Archipelago), *J. Geophys. Res.*, *110*, C11009, doi:10.1029/2005JC002922.

Laxon, S. W., et al. (2013), CryoSat-2 estimates of Arctic sea ice thickness and volume, *Geophys. Res. Lett.*, *40*, 732–737, doi:10.1002/grl.50193.

Leu, E., C. J. Mundy, P. Assmy, K. Campbell, T. Gabrielsen, M. Gosselin, T. Juul-Pedersen, and R. Gradinger (2015), Arctic spring awakening—Steering principles behind the phenology of vernal ice algal blooms, *Prog. Oceanogr.*, *139*, 151–170, doi:10.1016/j.pocean.2015.07.012.

Lizotte, M. P. (2001), the contributions of sea ice algae to Antarctic marine primary production, *Am. Zool.*, *41*, 57–73.

Losch, M., D. Menemenlis, J. M. Campin, P. Heimbach, and C. Hill (2010), On the formulation of sea-ice models: Part 1: Effects of different solver implementations and parameterizations, *Ocean Modell.*, *33*, 129–144, doi:10.1016/j.ocemod.2009.12.008.

Marshall, J., A. J. Adcroft, C. N. Hill, L. Perelman, and C. Heisey (1997), A finite-volume, incompressible Navier Stokes model for studies of the ocean on parallel computers, *J. Geophys. Res.*, *102*(C3), 5753–5766, doi:10.1029/96JC02,775.

Meiners, K. M., et al. (2012), Chlorophyll *a* in Antarctic sea ice from historical ice core data, *Geophys. Res. Lett.*, *39*, L21602, doi:10.1029/2012GL053478.

Meiners, K. M., et al. (2017), Antarctic pack ice algal distribution: Floe-scale spatial variability and predictability from physical parameters, *Geophys. Res. Lett.*, *44*, 7382–7390, doi:10.1002/2017GL074346.

Melbourne-Thomas, J., K. M. Meiners, C. J. Mundy, C. Schallenberg, K. L. Tattersall, and G. S. Dieckmann (2015), Algorithms to estimate Antarctic sea ice algal biomass from under-ice irradiance spectra at regional scales, *Mar. Ecol. Prog. Ser.*, *536*, 107–121, doi:10.3354/meps11396.

Melbourne-Thomas, J., K. M. Meiners, C. J. Mundy, C. Schallenberg, K. L. Tattersall, and G. S. Dieckmann (2016), Corrigendum: Algorithms to estimate Antarctic sea ice algal biomass from under-ice irradiance spectra at regional scales, *Mar. Ecol. Prog. Ser.*, *561*, 261, doi:10.3354/meps11396.

Melnikov, I. A., E. G. Kolosova, H. E. Welch, and L. S. Zhitina (2002), Sea ice biological communities and nutrient dynamics in the Canada Basin of the Arctic Ocean, *Deep Sea Res., Part I*, *49*(9), 1623–1649, doi:10.1016/S0967-0637(02)00042-0.

Michel, C., L. Legendre, S. Demers, and J.-C. Therriault (1988), Photoadaptation of sea-ice microalgae in springtime: Photosynthesis and carboxylating enzymes, *Mar. Ecol. Prog. Ser.*, *50*, 177–185.

Mock, T., and R. Gradinger (1999), Determination of Arctic ice algal production with a new in situ incubation technique, *Mar. Ecol. Prog. Ser.*, *177*, 15–26.

Monod, J. (1949), The growth of bacterial cultures, *Annu. Rev. Microbiol.*, *3*, 371–394, doi:10.1146/annurev.mi.03.100149.002103.

Mortensen, E., et al. (2017), A model-based analysis of physical and biological controls on ice algal and pelagic primary production in Resolute Passage, *Elem Sci. Anthropocene*, *50*, 39.

Nicolaus, M., C. Katlein, J. A. Maslanik, and S. Hendricks (2012), Changes in Arctic sea ice result in increasing light transmittance and absorption, *Geophys. Res. Lett.*, *39*, L24501, doi:10.1029/2012GL053738.

Perovich, D. K. (1996), The optical properties of sea ice, PhD thesis, *Monograph 96-1*, prepared for Office of Naval Research.

Perovich, D. K., T. C. Grenfell, J. A. Richter-Menge, B. Light, W. B. Tucker III, and H. Eicken (2003), Thin and thinner: Sea ice mass balance measurements during SHEBA, *J. Geophys. Res.*, *108*(C3), 8050, doi:10.1029/2001JC001079.

Proshutinsky, A., et al. (2001), The Arctic Ocean Model Intercomparison Project (AOMIP), *EOS*, *82*(51), 637–644.

Ricker, R., S. Hendricks, D. K. Perovich, V. Helm, and R. Gerdes (2015), Impact of snow accumulation on CryoSat-2 range retrievals over Arctic sea ice: An observational approach with buoy data, *Geophys. Res. Lett.*, *42*, 4447–4455, doi:10.1002/2015GL064081.

Ricker, R., S. Hendricks, F. Girard-Ardhuin, L. Kaleschke, C. Lique, X. Tian-Kunze, M. Nicolaus, and T. Krumpen (2017), Satellite-observed drop of Arctic sea ice growth in winter 2015–2016, *Geophys. Res. Lett.*, *44*, 3236–3245, doi:10.1002/2016GL072244.

Saenz, B. T., and K. R. Arrigo (2014), Annual primary production in Antarctic sea ice during 2005–2006 from a sea ice state estimate, *J. Geophys. Res. Oceans*, *119*, 3645–2678, doi:10.1002/2013JC009677.

Saha, S., et al. (2014), The NCEP Climate Forecast System Version 2, *J. Clim.*, *27*(6), 2185–2208, doi:10.1175/JCLI-D-12-00823.1.

Sarthou, G., K. R. Timmermans, S. Blain, and P. Tréguer (2005), Growth physiology and fate of diatoms in the ocean: A review, *J. Sea Res.*, *53*(1–2), 25–42, doi:10.1016/j.seares.2004.01.007.

Schünemann, H., and I. Werner (2005), Seasonal variations in distribution patterns of sympagic meiofauna in Arctic pack ice, *Mar. Biol.*, *146*(6), 1091–1102, doi:10.1007/s00227-004-1511-7.

Semtner, A. J. J. (1976), A model for the thermodynamic growth of sea ice in numerical investigations of climate, *J. Phys. Oceanogr.*, *6*, 379–389.

Serreze, M. C., J. A. Maslanik, T. A. Scambos, F. Fetterer, J. Stroeve, K. Knowles, C. Fowler, S. Drobot, R. G. Barry, and T. M. Haran (2003), A record minimum Arctic sea ice extent and area in 2002, *Geophys. Res. Lett.*, *30*(3), 1110, doi:10.1029/2002GL016,406.

Serreze, M. C., M. M. Holland, and J. Stroeve (2007), Perspectives on the Arctic's Shrinking Sea-Ice Cover, *Science*, *315*(5818), 1533–1536, doi:10.1126/science.1139,426.

Sibert, V., B. Zakardjian, F. Saucier, M. Gosselin, M. Starr, and S. Senneville (2010), Spatial and temporal variability of ice algal production in a 3D ice–ocean model of the Hudson Bay, Hudson Strait and Foxe Basin system, *Polar Res.*, *29*(3), 353–378, doi:10.1111/j.1751-8369.2010.00184.x.

Smith, R. E. H., M. Gosselin, and S. Taguchi (1997), The influence of major inorganic nutrients on the growth and physiology of high Arctic ice algae, *J. Mar. Syst.*, *110*, 63–70.

Søreide, J. E., M. L. Carroll, H. Hop, W. G. Ambrose Jr., E. N. Hegseth, and S. Falk-Petersen (2013), Sympagic-pelagic-benthic coupling in Arctic and Atlantic waters around Svalbard revealed by stable isotopic and fatty acid tracers, *Mar. Biol. Res.*, *9*(9), 831–850.

Steiner, N., M. Harder, and P. Lemke (1999), Sea-ice roughness and drag coefficients in a dynamic-thermodynamic sea-ice model for the Arctic, *Tellus, Ser. A*, *51*, 964–978, doi:10.1034/j.1600-0870.1999.00,029.x.

Stroeve, J., M. M. Holland, W. Meier, T. Scambos, and M. Serreze (2007), Arctic sea ice decline: Faster than forecast, *Geophys. Res. Lett.*, *34*, L09501, doi:10.1029/2007GL029,703.

Stroeve, J. C., V. Kattsov, P. Barret, M. Serreze, T. Pavlova, M. Holland, and W. N. Meier (2012a), Trends in Arctic sea ice extent from CMIP5, CMIP3 and observations, *Geophys. Res. Lett.*, *39*, L16502, doi:10.1029/2012GL052,676.

Stroeve, J. C., M. C. Serreze, M. M. Holland, J. E. Kay, J. Maslanik, and A. P. Barret (2012b), The Arctic's rapidly shrinking sea ice cover: A research synthesis, *Clim. Change*, *110*(3–4), 1005–1027.

Sturm, M., J. Holmgren, and D. K. Perovich (2002), Winter snow cover on the sea ice of the Arctic Ocean at the Surface Heat Budget of the Arctic Ocean (SHEBA), *J. Geophys. Res.*, *107*(C10), 8047, doi:10.1029/2000JC000400.

Tedesco, L., M. Vichi, J. Haapala, and T. Stipa (2010), A dynamic Biologically Active Layer for numerical studies of the sea ice ecosystem, *Ocean Modell.*, *35*(1–2), 89–104, doi:10.1016/j.ocemod.2010.06.008.

Tilling, R. L., A. Ridout, A. Shepherd, and D. J. Wingham (2015), Increased Arctic sea ice volume after anomalously low melting in 2013, *Nat. Geosci.*, *8*(8), 643–646, doi:10.1038/ngeo2489.

Timco, G. W., and R. P. Burden (1997), An analysis of the shapes of sea ice ridges, *Cold Reg. Sci. Technol.*, *25*, 65–77.

Tremblay, J.-É., K. Simpson, J. Martin, L. Miller, Y. Gratton, D. Barber, and N. M. Price (2008), Vertical stability and the annual dynamics of nutrients and chlorophyll fluorescence in the coastal, southeast Beaufort Sea, *J. Geophys. Res.*, *113*, C07S90, doi:10.1029/2007JC004547.

Vancoppenolle, M., and L. Tedesco (2017), Numerical models of sea ice biogeochemistry, in *Sea Ice*, edited by D. N. Thomas, pp. 492–515, John Wiley & Sons, Ltd, Chichester, U. K., doi: 10.1002/9781118778371.ch20.

Vancoppenolle, M., et al., (2011), Assessment of radiation forcing data sets for large-scale sea ice models in the Southern Ocean, *Deep Sea Res., Part II*, *58*(9–10), 1237–1249, doi:10.1016/j.dsr2.2010.10.039.

Vancoppenolle, M., et al. (2013), Role of sea ice in global biogeochemical cycles: emerging views and challenges, *Quat. Sci. Rev.*, *79*, 207–230, doi:10.1016/j.quascirev.2013.04.011.

Wassmann, P., et al. (2006), Food webs and carbon flux in the Barent Sea, *Prog. Oceanogr.*, *71*(2–4), 232–287.

Webb, W. L., M. Newton, and D. Starr (1974), Carbon dioxide exchange of *Alnus rubra*, *Oecologia*, *17*(4), 281–291, doi:10.1007/BF00345747.

Welch, H. E., and M. A. Bergmann (1989), Seasonal development of ice algae and its prediction from environmental factors near Resolute, N.W.T., Canada, *Can. J. Fish. Aquat. Sci.*, *46*, 1793–1804.

Werner, I., and R. Gradinger (2002), Under-ice amphipods in the Greenland Sea and Fram Strait (Arctic): Environmental controls and seasonal patterns below the pack ice, *Mar. Biol.*, *140*(2), 317–326, doi:10.1007/s00227-001-0709-1.

Zeebe, R. E., H. Eicken, D. H. Robinson, D. Wolf-Gladrow, and G. S. Dieckmann (1996), Modeling the heating and melting of sea ice through light absorption by microalgae, *J. Geophys. Res.*, *101*(C1), 1163–1181, doi:10.1029/95JC02687.